

Structural, Opto-electronic and Electrical Properties of pure NiO nanostructures and Ga-Li co-doped NiO

M.Sc. Thesis

By
Sayak Datta



**DISCIPLINE OF PHYSICS
INDIAN INSTITUTE OF TECHNOLOGY INDORE
June 2022**

Structural, Opto-electronic and Electrical Properties of pure NiO nanostructures and Ga-Li co-doped NiO

A THESIS

*Submitted in partial fulfillment of the
requirements for the award of the degree
of
Master of Science*

by
Sayak Datta



**DISCIPLINE OF PHYSICS
INDIAN INSTITUTE OF TECHNOLOGY INDORE**

June 2022



INDIAN INSTITUTE OF TECHNOLOGY INDORE

CANDIDATE'S DECLARATION

I hereby certify that the work which is being presented in the thesis entitled **Structural, Opto-electronic and Electrical Properties of pure NiO nanostructures and Ga-Li co-doped NiO**

in the partial fulfillment of the requirements for the award of the degree of **MASTER OF SCIENCE** and submitted in the **DISCIPLINE OF PHYSICS, Indian Institute of Technology Indore**, is an authentic record of my own work carried out during the time period from August 2020 to June 2022 under the supervision of Dr. Somaditya Sen, Associate Professor, Discipline of Physics, Indian Institute of Technology Indore.

The matter presented in this thesis has not been submitted by me for the award of any other degree of this or any other institute.

Sayak Datta 06/06/2022
Signature of the student with date
SAYAK DATTA

This is to certify that the above statement made by the candidate is correct to the best of my/our knowledge.

Somaditya Sen 6/6/2022
Signature of the Supervisor of
M.Sc. thesis (with date)
DR. SOMADITYA SEN

SAYAK DATTA has successfully given his/her M.Sc. Oral Examination held on **06/06/2022**.

Somaditya Sen 6/6/2022

Signature(s) of Supervisor(s) of MSc thesis
Date:

Mandana Datta
Convener, DPGC
Date: 08/06/2022

Rajesh Kumar
Signature of PSPC Member
Prof. Rajesh Kumar
Date: **06/06/2022**

Krushna Mavani
Signature of PSPC Member
Prof. Krushna Mavani
Date: **06/06/2022**

***DEDICATED TO
MY TEACHERS AND
MY FAMILY***

ACKNOWLEDGEMENT

This thesis represents the final stage in completing my MSc. degree. This journey would not have been possible without the constant encouragement, motivation, and support of a few people. First and foremost, I want to express my sincere gratitude to my thesis supervisor, Dr. Somaditya Sen, for providing me with the opportunity to do research work and also for providing me with insightful remarks, direction, and unwavering encouragement and support throughout my MSc. years. His dynamism and excitement for work has inspired me to work even harder and more passionately. I would also like to express my sincere thanks to my PSPC members, Prof. Rajesh Kumar and Prof. Krushna Mavani for evaluating and providing me with valuable feedback regarding my project work. I also want to extend my heartfelt thanks to the Department of Physics, IIT Indore especially SMART Lab and SIC for providing me with the necessary laboratory equipments and favourable environment for carrying out research work and exploring new ideas. Last but not the least thanks to all my lab members especially Ms. Koyal Suman Samantaray, Mr. Prashant Kumar Mishra, Ms. Maneesha P, Mr. Suresh Chandra Baral and Mr. Mukul Kumar for their constant support and guidance right from the beginning and all my friends for helping me and co-operating with me in completing this thesis. Lastly, I want to acknowledge the help of my parents for their unconditional love and care throughout the years and always encouraging and supporting me in every walk of life. Hence, I can safely conclude that this project would not have been completed unless the above honourable people have helped me.

SAYAK DATTA

ABSTRACT

Nickel oxide (NiO) nanoparticles along with Gallium (Ga) and Lithium (Li) doping of 1% have been synthesized by sol-gel method using nickel nitrate $[\text{Ni}(\text{NO}_3)_2 \cdot 6\text{H}_2\text{O}]$, Gallium nitrate $[\text{Ga}(\text{NO}_3)_3]$ and Lithium nitrate $[\text{LiNO}_3]$ in appropriate proportions. NiO nanostructures have also been synthesized by hydrothermal method using Nickel chloride $[\text{NiCl}_2 \cdot 6\text{H}_2\text{O}]$, DI (Deionized) water, ethanol and ammonium hydroxide. The synthesized samples were then subjected to characterizations like XRD, Raman Spectroscopy, UV-VIS Spectroscopy, FESEM, EDX and conductivity studies. Rietveld refinement was done for all the samples and the variation in bond length, bond angle, lattice parameters, crystallite size and lattice strain was calculated. Raman spectroscopy revealed different phonon modes and their frequencies which can be directly correlated with the XRD analysis. As reported in the literature, NiO can be both direct and indirect band gap semiconductor. Direct band gap of about 3.4-3.8 eV and indirect band gap in the range of 2.8-3.3 eV was calculated from UV-Vis data. FESEM and EDX data gave the appropriate particle size and morphology of the samples. Pressure dependent and magnetic field dependent conductivity studies revealed quite astounding results and enhancement in the conductivity with Li and Ga doping in NiO.

TABLE OF CONTENTS

LIST OF FIGURES	X
Chapter 1: Introduction	1
1.1 Introduction and Background.....	2
1.2 Fundamental Properties	3
1.3 Applications	7
Chapter 2: Material Synthesis and Experimental Method	11
2.1 Experimental Techniques: Synthesis Routes	12
2.2 Sample Preparation: Hydrothermal Method	13
2.3 Sample Preparation: Sol-Gel Method	15
2.4 Synthesis of Ga/Li co-doped NiO	17
2.5 Characterization Techniques	18
2.5.1 X-ray Diffraction	18
2.5.2 Raman Spectroscopy	22
2.5.3 UV-VIS Spectroscopy	25
2.5.4 Field emission scanning electron microscopy	27
2.5.5 Energy Dispersive X-ray Spectroscopy	29
Chapter 3: Results and Discussion	30
3.1 Structural, Opto-electronic and Electrical Studies of NiO nanostructures.....	31
3.1.1 XRD Diffraction	31
3.1.2 Raman Spectroscopy	32
3.1.3 UV-Visible Spectroscopy.....	33
3.1.4 FESEM and EDX Data Analysis	35
3.2 Structural, Opto-electronic and Electrical Studies of Ga/Li co-doped NiO	37

3.2.1 X-ray Diffraction	38
3.2.2 Raman Spectroscopy	41
3.2.3 UV-Visible Spectroscopy.....	43
3.2.4 Pressure dependent I-V characteristics	45
3.3 Summary of the chapter.....	47
Chapter 4: Conclusion	48
4.1 Conclusions and Scope for Future Work	49
References	50

LIST OF FIGURES

Figure 1.1: Crystal Structure of Nickel Oxide (fcc lattice)	3
Figure 2.1: Schematic diagram for the steps involved in Hydrothermal method	13
Figure 2.2: Experimental set-up for Hydrothermal method including (a) 200 ml Teflon lined Stainless Steel Autoclave (b) Thermal chamber for heat treatment	15
Figure 2.3: Schematic Diagram of Sol-Gel Process	15
Figure 2.4 Muffle Furnace used for annealing the prepared samples	17
Figure 2.5: X-ray diffraction through Bragg's reflection in the atomic planes	18
Figure 2.6 Schematic Diagram of a X-ray Diffractometer	19
Figure 2.7 (a) Bruker D2 Phaser X-ray Diffractometer (b) Inside view of X-ray Diffractometer	20
Figure 2.8 Schematic diagram showing Raman scattering	22
Figure 2.9 Schematic representation of Raman spectrometer	23
Figure 2.10 (a) Schematic representation of UV-Visible Spectrophotometer (b) Schematic diagram of bands in solids	25
Figure 2.11 Experimental Set-up for UV-Visible Spectrophotometer	26
Figure 2.12 (a) Schematic Diagram of Field Emission Scanning Electron Microscope (b) #1 Complete arrangement of the FESEM. #2 Connected computer systems running user-friendly software. #3 EDX measurement system. #4 It is a complete set of gold sputtering. #5 Enlarged part of the sample holder of the gold sputtering system.	27
Figure 3.1 (a) X-ray Diffraction Patterns of NiO nanostructures (b) Variation of Crystallite size and Lattice Strain (c) Variation of lattice parameters (d) Variation in bond length (e) Variation in bond angle	32
Figure 3.2 Rietveld refinement plot of the NiO nanostructures	32
Figure 3.3 The room temperature Raman spectra of NiO nanostructures annealed at 450 °C.	33
Figure 3.4 (a) Absorption spectra of UV-Vis for NiO nanostructures (b) Variation in the band gap energy (c) Variation in the Urbach energy.	35
Figure 3.5 (a) FESEM and EDX Data of NiO nanosheet (C1)	36
Figure 3.5 (b) FESEM and EDX Data of NiO microsphere (C2)	36
Figure 3.5 (c) FESEM and EDX Data of NiO flake-flower (C3)	36
Figure 3.6 (a) XRD Pattern of $\text{Ni}_{0.9844}(\text{Ga}_{1-x}\text{Li}_x)_{0.0156}\text{O}$ for $x=0, 0.25, 0.5, 0.75$ and 1 (b) Variation of Crystallite size and Lattice Strain (c) Variation of lattice parameters (d) Variation in bond length (e) Variation in bond angle.	40

Figure 3.7 Rietveld refinement of pure NiO from the above series $\text{Ni}_{0.9844}(\text{Ga}_{1-x}\text{Li}_x)_{0.0156}\text{O}$ annealed at 600 °C	40
Figure 3.8 Raman Spectra of $\text{Ni}_{0.9844}(\text{Ga}_{1-x}\text{Li}_x)_{0.0156}\text{O}$ annealed at 600 °C	42
Figure 3.9 Variation in the phonon frequency and peak width with different doping concentrations of $\text{Ni}_{0.9844}(\text{Ga}_{1-x}\text{Li}_x)_{0.0156}\text{O}$.	42
Figure 3.10 (a) Tauc plot for direct band gap (b) Variation in direct band gap energy (c) Tauc plot for indirect band gap (d) Variation in indirect band gap energy (e) Variation in Urbach energy.	44
Figure 3.11 (a) Uni-axial Hydraulic Press for making pellets (b) Keithley 2450 Source Meter	45
Figure 3.12 Pressure dependent current vs voltage plots (I-V characteristics) for $\text{Ni}_{0.9844}(\text{Ga}_{1-x}\text{Li}_x)_{0.0156}\text{O}$.	46

Chapter 1

Introduction

1.1 Introduction and Background: -

In the present world, metal oxides play an important role in our everyday life [1]. It finds its application in diverse areas such as in modern electronic devices, in the manufacture of fuel cells, as corrosion resistant coatings and as catalysts in various chemical reaction [1]. Metal oxides are extremely important for human beings and contemporary industries, as they serve as an accessory in many compounds of daily application. In addition, they serve as a raw material in chemical laboratories to obtain bases and other compounds, since their abundance [2] makes them much easier to obtain and handle effectively. Distinct chemical and physical properties are characteristic of nanoparticles because of their smaller dimension and dense edges [3]. Materials in the form of nanoparticles have attracted interest for physical[4], chemical[4], catalytic[4], magnetic[4], and optical applications[4] in the recent decades. Among different categories of nanoparticles, transition metals such as Ni, Co, and Fe are gaining special interest because of their potential properties and applications in opto-electronics[5], electronics[5], sensing[5], medicine[5], and catalysis[5]. When compared to their bulk form, NPs have numerous physicochemical characteristics. This is because with decrease in size, surface to volume ratio increases and quantum effects become more pronounced [5], [6]. This increase in surface to volume ratio modifies the thermal, mechanical and catalytic properties of a material [6].

In the last decade, Nickel oxide (NiO) have gained a growing attention from the scientific community because they are cheap, easy to produce and isolate, and they could be employed in many applications. It is one among few p-type semiconductors [7], whose research has gotten a lot of attention in recent years because of its possible applications in a variety of new domains of technology.

1.2 Fundamental properties: -
Crystal structure: -

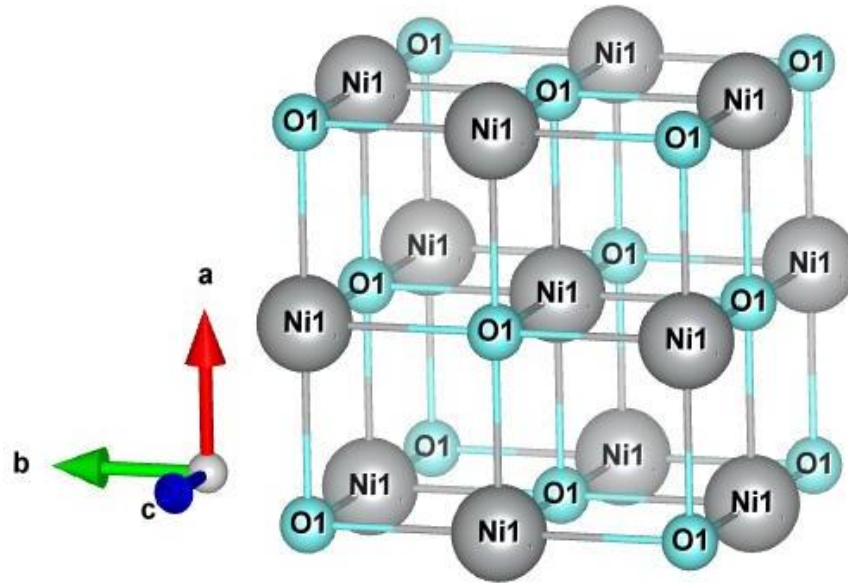


Figure 1.1 Crystal Structure of Nickel Oxide (fcc lattice)

NiO nano powders have a black colour and a cubic structure with $Fm\bar{3}m$ symmetry [Figure 1.1]. NiO has the same structure as NaCl, with octahedral Ni^{2+} and O^{2-} sites[8]. The rock salt structure is a simple structure to understand. The Ni:O ratio is not usually 1:1 in NiO, as it is in many other binary metal oxides[8]. This non-stoichiometry in NiO causes a color shift, with stoichiometrically correct NiO turning green and non-stoichiometrically correct NiO turning black [9]. In contrast to NiO, it is a unique 3d transition-metal monoxide that crystallizes in the rock salt structure with substantially higher symmetry [7].

Each unit cell has four formula units. The ions Ni^{2+} and O^{2-} are both octahedrally coordinated [10]. Six O^{2-} ions in the corners of an octahedral form are sixfold coupled with Ni^{2+} ions. The Ni^{2+} and O^{2-} ions occupy Wykoff's locations 4b (0,1/2, 0) and 4e (0, y, 1/4), respectively. The unit cell parameters are as follows: $a = b = c = 4.1684 \text{ \AA}$, $\alpha = \beta = \gamma = 90^\circ$, volume = 72.4283. The bond distance of NiO is 2.0842 \AA [11].

According to Density Function Theory (DFT), NiO can be both a direct bandgap of 3.56 eV and indirect bandgap semiconductor of 3.12 eV [12][13]. Energy bandgap is the difference between the energy levels of the valence band maxima (VB) and the conduction band minima (CB). Ni 3d orbitals are used to infer both valence and conduction band states [14]–[16]. The bandgap has been measured in the region of 3.5–4 eV in experiments[12], [13]. In some circumstances, theory and experiment coincide. Native defects are common in semiconductors and have a big impact on their electrical characteristics. In a systematic investigation, the optoelectronic properties of stoichiometric NiO, oxygen-rich NiO with Ni vacancies (NiO:V_{Ni}), and Ni-rich NiO with O vacancies were compared (NiO:Vo). Both NiO systems with vacancies display gap states, according to computational research. The majority of NiO:Vo gap states are Ni 3d states, whereas NiO:V_{Ni} gap states are a mix of Ni 3d and O 2p states. The absorption spectra of the NiO:V_{Ni} sample show prominent defect-induced features below 3.0 eV when compared to NiO and NiO:Vo samples. Gap states in the electronic density of states cause the increase in sub-gap absorptions in NiO:V_{Ni}. The relationship between native vacancy defects and NiO electrical and optical characteristics is explored for comparable vacancy levels,

Morphology and particle size have significant effect on the capacitance. The conductivity increases as particle size decreases. The morphology is intimately connected to porosity and surface area [3]. High surface area and porosity allow for easy ion diffusion, resulting in high capacitance. NiO are obtained in various structural forms which includes nanoparticle, nanoflakes, nanowire, nanoflower, nanosheet, nanorods, nanobelt and so on [3].

Optical Properties: -

Optical properties of metal oxides are important parameters for optoelectronic devices. At 2.37 eV, NiO nanoparticles produce a strong

green band that accounts for 80% of the integrated intensity of PL spectra. This strange phenomenon is explained by the recombination of photogenerated holes that are trapped in the oxygen's deep level vacancy with electrons in a shallow level just below the conducting band. Stoichiometric NiO emissions in the UV band at 346 nm (3.58 eV) have been reported in pure NiO [13]. The emission bands of this collection of nanoparticles range from ultraviolet to visible, suggesting that NiO nanoparticles are highly defective. DLE green luminescence is a defect-related green luminescence of NiO nanoparticles that dominates the PL spectra about 520 nm (2.38 eV). UV emission from the near-band-edge (NBE) is moderate but widespread at 333–357 nm (3.47–3.72 eV). Exciton recombination causes UV emission, which corresponds to NiO's NBE transition [17], but structural flaws such as interstitial defects and oxygen vacancies induce DLE in the visible range, which is classified as DLE1 through DLE3.

The electron hole recombination process is avoided when microscopic particles having substantial nickel vacancies on the surface are excited, resulting in decreased intensity. In big particles, thermal annealing induces more electron hole recombination, resulting in higher intensity UV band emission. Because all NiO nanoparticles emit red light at room temperature, they could be employed in optoelectronic nanodevices that emit red light, such as light-emitting diodes or laser diodes [17].

Materials with a high absorption coefficient in the visible region are ideal for this purpose. As solar cells with an absorber layer, NiO films are quite useful. When compared to the bulk equivalent, the band gap of NiO nanostructures is red shifted [15]. Various band gap ranges between 3.5 and 4.0 eV have been observed. A bandgap of 3.4 eV was found for well-aligned arrays of NiO nanoplates [12]. As a result, NiO absorbs light from the visible to the ultraviolet spectrum. Using diffuse reflectance spectroscopy, the NiO nanoparticle was determined to have an optical

band gap of around 4.47 eV, and the photoluminescence (PL) emission spectra of our synthesized sample revealed a prominent peak at 3.65 eV ascribed to the band edge transition.

Absorption techniques are commonly used to explore the optical characteristics of NiO nanoparticles. Near-band-edge (NBE) and deep-level-emission (DLE) in nickel oxide (NiO) nanoparticles of various sizes are influenced by nickel/oxygen vacancies and interstitial defects. Excitonic recombination at NiO's near-band-edge (NBE) transition induced ultraviolet (UV) emission, while structural defects like interstitial defects and oxygen vacancies induced deep-level-emission (DLE) in the visible range.

Vibrational properties: -

Raman spectroscopy examines the phonon vibrations of a lattice. Vibrational properties and spin phonon coupling are studied by this technique and depends on inelastic scattering of a monochromatic light [18]. Under visible and UV illumination, the Raman spectra of NiO is shown. The TO and LO phonon modes are represented by faint peaks in the ranges of 350 cm^{-1} to 410 cm^{-1} and 520 cm^{-1} to 580 cm^{-1} , respectively. 2TO (738 cm^{-1}), 2LO (1142 cm^{-1}), and a combination of TO and LO (913 cm^{-1}) phonon modes are ascribed to the stronger second-order peaks.

Electrical properties: -

The microstructural defects like interstitial defects and nickel vacancies determine the electrical conductivity of NiO. The size of nanoparticle influences the electrical properties. The scattering effect at grain boundary is reduced when the grains are bigger in size with less boundaries, thereby effecting the electrical conductivity [3]. NiO is a crucial component in nanoelectronics. A material's conductivity is influenced by structural changes such as grain size, grain boundary, and dopant type [19], [20]. As

a result, different synthesis processes, annealing temperatures, and growth conditions have an effect on NiO's electrical properties. Temperature increases NiO's electrical conductivity, mobility, and carrier concentration [21]. Altering the stoichiometry and crystallinity of NiO films during the deposition process, which are impacted by pH, ion pressure, and concentration during film deposition, can also modify electrical characteristics [22].

Magnetic Properties: -

Magnetic nanoparticles are ubiquitously used in conducting paints, rechargeable batteries, chemical catalyst, optoelectronics, magnetic recording media, magnetic resonance imaging, etc. The physical properties of bulk are different from the nanoparticles. As a bulk substance, nickel oxide is magnetic [3]. At Neel temperature $T_N = 523$ K, it undergoes an antiferromagnetic ordering transition, in which Ni-ions planes perpendicular to (1,1,1) align their magnetic moments parallel to one other, and consecutive planes with ordered moments are antiparallel, resulting in type II anti-ferromagnetism [3]. In this approach, Ni-O-Ni bonds are antiferromagnetic. NiO exhibits a rock-salt crystal cubic shape in the paramagnetic phase above the Neel temperature [3].

1.3 Applications: -

NiO is a promising candidate for optical and electronic devices, among other things. Natural resources abound, and it is non-toxic and thermally stable. Its electrochemical characteristics and low-cost manufacturing add to its application. NiO nanoparticles can be used for a variety of applications, including high-temperature superconductors, emitters, solar cells, gas sensors, magnetic storage media, varistors and catalysis, antimicrobial activities, photoelectrochemical cells, and Li-ion batteries [23].

Solar cells and light-emitting diodes (LED's): -

Photovoltaic applications have made extensive use of NiO [24]. Solar dye-sensitized cells and light-emitting diodes could benefit from NiO thin films. The scientific community is becoming increasingly interested in NiO as a clean and cost-effective energy source. NiO can be used as a solar cell absorber to convert solar energy into electricity directly. Although NiO-based solar cells have a theoretical efficiency of 22.1 percent, the maximum practical efficiency so far is 2.30 percent. As a result, much more research is required to improve efficiency. OLEDs (organic light-emitting diodes) are a form of organic light-emitting diode [25]. NiO is a fast material. NiO is employed as a hole injection layer in several diodes to overcome the hole injection barrier[26]. The stoichiometry of NiO has many defects (V_O , V_{Ni}). These defects act as an additional energy level within the bandgap NiO which may result in increasing the hole injection efficiency[27]. Also, good quality nanostructures with a high surface area may improve the effectiveness of NiO based solar cells.

Photocatalytic activity: -

Water pollution is a major problem in today's world because many organic compounds in wastewater are poisonous and unable to degrade by themselves. Under solar UV or visible light, semiconductor catalysts can effectively breakdown these chemical molecules with minimal effort. Because of its low bandgap, NiO is a potential material for organic contaminant degradation and water splitting[28]. Under visible light exposure, NiO generates electron-hole pairs. This process also generates hydroxyl radicals (*HO) from water, which have the ability to mineralize organic compounds [29]. In the NiO water splitting process, the majority carriers, holes, oxidize water to O_2 , while the photogenerated minority electron charge carriers reduce water to H_2 . The addition of a little H_2O_2 to

the solution containing NiO nanoparticles improves their photocatalytic activities. NiO's photocatalytic capabilities are highly influenced by its shape and size [28]. For photocatalytic degradation of organic dyes, NiO nanowires have gotten a lot of attention [29].

Supercapacitors and electrodes for lithium-ion batteries: -

Because of its environmental friendliness and great capacitive properties, NiO is regarded as an excellent electrode for supercapacitor applications. The electrochemical characteristics of NiO are influenced by its morphology and size [30], [31]. The high specific capacitance is due to the mesoporous structure and surface area. Li-ion batteries are a popular type of battery that may be able to meet the rising demand for laptop and cell phone batteries. Metal oxide-based materials, such as Fe₂O₃, Fe₃O₄, CoO, Co₃O₄, Mn_xO_y, Cu₂O/CuO, NiO, Cr₂O₃, RuO₂, and MoO₃/MoO₃, have been developed, with theoretical mAh g⁻¹ capacities ranging from 500 to 1200 mAh g⁻¹. Transition metal-based phosphides, nitrides, and sulfides with capacities ranging from 500 to 1800 mAh g⁻¹ have also been developed. These materials, on the other hand, have issues including significant potential hysteresis and unstable SEI production, making them less desirable for Li-ion battery operations [32].

Sensing Applications: -

NiO has been used to sense numerous compounds such as CO, HCN, and glucose due to its superior surface conductivity. The amount of surface area on which sensitivity is controlled is crucial. The sensing characteristics of nanostructured NiO are greatly affected by the high surface to volume ratio. As a result, shape and size are essential considerations. According to Aslani et al., when comparing cloud-like morphologies of NiO to other morphologies, those with a high surface to volume ratio have a better responsiveness and detection limit [33]. NiO nanostructures have a large specific surface area, which makes them more

sensitive to HCN detection. Changes in chemical reactivity of distinct crystallographic planes explain variations in sensitivity.

Magnetic Applications: -

Magnetic nanoparticles have a wide range of uses, including magnetic fluids [34], magnetic energy storage, and information storage [35]. They are used in enhancing the capacity of magnetic tapes, computer hard discs and in magneto-resistance sensors[36]–[38]. Magnetic nanoparticles are utilized as contrast agents to increase contrast in MRI [36]. They're also utilized to deliver drugs to precise locations. Nanoparticle ferrofluid is utilized to treat cancers [36]–[39].

Chapter 2

Materials and Experimental Methods

2.1 Experimental Techniques: Synthesis Routes

Nanoparticle applications are influenced not only by their attributes (size, shape, and structure), but also by the synthesis process used. The physiochemical properties of NiO nanoparticles are determined by a variety of ways, which in turn determine their electrochemical properties.

Various methods for synthesizing nanocrystalline NiO from various precursor materials have been reported in the literature. Some technically assisted methods, such as spray pyrolysis, template process, microwave assisted method, and solvothermal method, have been reported in addition to simple methods such as sol-gel processes, thermal decomposition, chemical routes, and precipitation methods[40].

Primarily there are 2 methods for synthesizing NiO NPs which include top-down approach and bottom-up approach.

1. Synthesis of NPs using Top-Down Approach: This method is composed of a number of synthetic methods that make NPs by removing portions of a bulk substrate. Chemical, electrochemical, and mechanical procedures are some of the methods for removing parts from bulk materials [40], [41]. The substance of the bulk substrate and the required NP sizes determine which approach is used. However, this method does not provide you complete control over particle size. To create nanosized domains, the top-down method is extended, and mechanical removal techniques are combined with electrochemical and chemical techniques.

Laser ablation, chemical vapor deposition (CVD), and electro deposition are the most common top-down nanoparticle manufacturing processes [41].

2. Synthesis of NPs using Bottom-Up Approach: This method uses a variety of synthetic techniques to create bigger and more complex systems by mounting components on a base substrate while preserving good molecular structure. Surfactants are used to achieve significant adhesive forces between the surface layer and the base substrate which is the

primary requirement for this fabrication process [40], [41]. Metallic oxides and metallic salts are used as precursors for the reactions in bottom-up protocols. Using the right solvent and reducing agent, these salts or oxides are eventually converted to metallic nanoparticles.

Sol-gel method, spray pyrolysis, thermolysis, and micro-emulsion are the most often used bottom-up techniques [41].

2.2 Sample Preparation: Hydrothermal Method

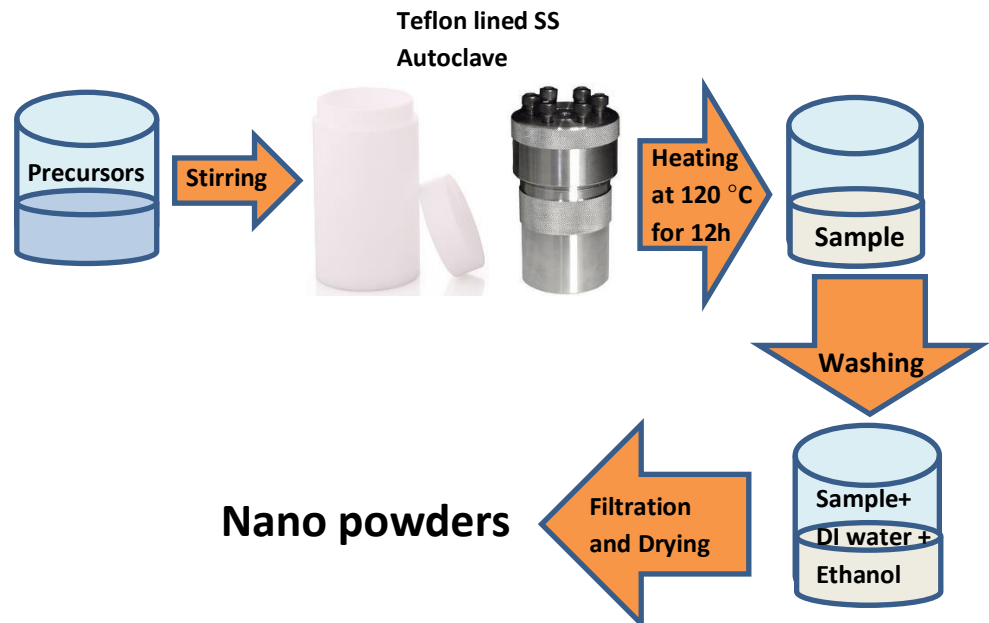


Figure 2.1. Schematic diagram for the steps involved in Hydrothermal method

1. NiO nanosheet

The sample was synthesized using hydrothermal method. In this process, a light-green solution was obtained dissolving 3 g of nickel chloride hexahydrate ($\text{NiCl}_2 \cdot 6\text{H}_2\text{O}$) in 100 ml deionised water. In order to adjust the solution pH to a value of 10, ammonia solution was added under magnetic stirring. After that, for hydrothermal treatment, the solution was taken into an autoclave of capacity 200 ml [Figure 2.2 (a)]. The

hydrothermal process was carried out in the thermal chamber for 12 hrs at a temperature of 120 °C. [Figure 2.2 (b)] and then naturally cooled to ambient temperature. In order to eliminate the impurities and unreacted reagents, the precipitate was later washed 5 times with DI water and ethanol, and the products were recovered through filtration. The precipitate was dried overnight at 45° C and annealed at 400° C for 2 hrs to finally obtain NiO nanosheets.

2. NiO microsphere

The sample was synthesized using hydrothermal method. 1g nickel chloride hexahydrate ($\text{NiCl}_2 \cdot 6\text{H}_2\text{O}$) and 1 ml ammonia solution were dissolved in 20 ml DI water for sample preparation. The solution was then mixed with 3g of glucose and stirred for 15-20 mins. The resulting solution was taken into a 200 mL Teflon-lined SS autoclave and heated for 12 hrs at 120 °C in the thermal chamber, and then naturally cooled to ambient temperature. The product was washed with DI water and ethyl alcohol many times before recovering it through filtration. Upon drying at 60° C for 6 hrs, the black powder left was annealed at 450°C for 2 hrs to finally obtain NiO microspheres.

3. NiO flake-flower

Typically, in a hydrothermal procedure, 1 g of $\text{NiCl}_2 \cdot 6\text{H}_2\text{O}$ was added into a solution composed of 25 ml of ethanol and 25 ml of DI water by volume[42]. Then, 0.5 g PVP (Polyvinylpyrrolidone) and 20 ml of Ethylene Glycol were added into the mixture under magnetic stirring [42]. In order to adjust the solution pH to a value of 10, ammonia solution was added. After that, a homogeneous solution was formed by magnetically stirring the mixture for 30 min and then taken into a Teflon-lined SS autoclave of capacity 200 mL and kept in thermal chamber for 12 hrs at 120 °C. The green sample was collected through filtration and washed with pure water and ethanol for a number of times, after cooling the

autoclave to room temperature. On drying at 60 °C for 10 h, the product was obtained by annealing at 450 °C for 2 h.

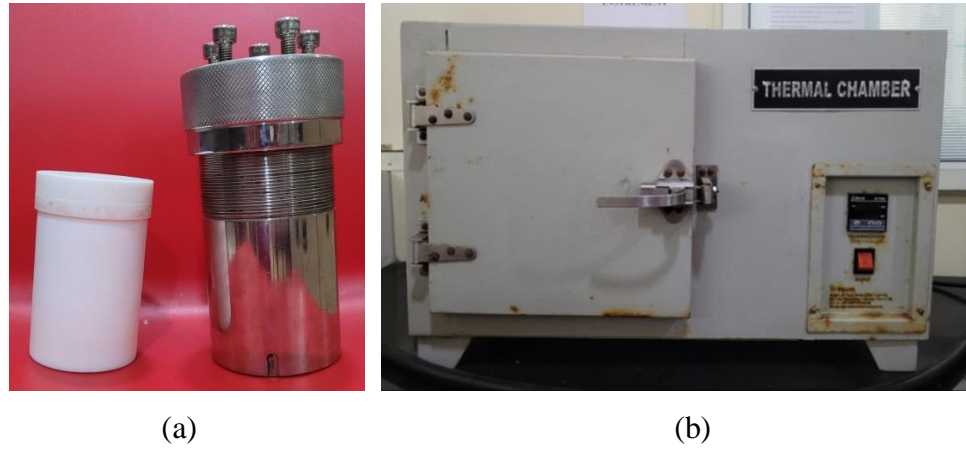


Figure 2.2 Experimental set-up for Hydrothermal method including (a) 200 ml Teflon lined Stainless Steel Autoclave (b) Thermal chamber for heat treatment.

2.3 Sample Preparation (Sol-Gel Method)

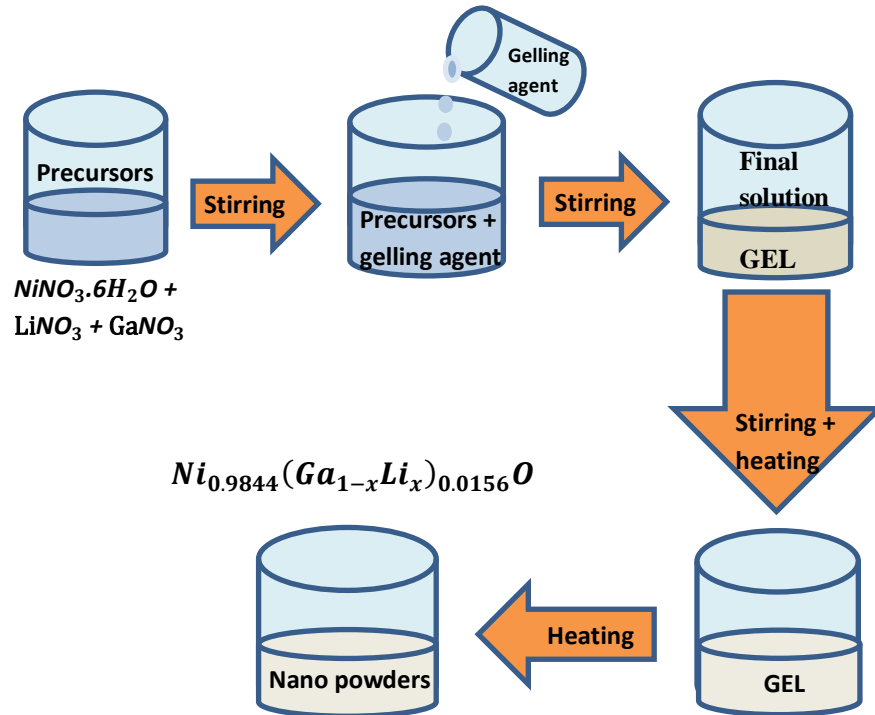


Figure 2.3: Schematic Diagram of Sol-Gel Process

The synthesis and characterization for $\text{Ni}_{0.9844}(\text{Ga}_{1-x}\text{Li}_x)_{0.0156}\text{O}$ are briefly discussed in this chapter. A modified sol-gel process is used to synthesis the samples, which is then followed by successive high-temperature annealing. The following characterization techniques were used to investigate material properties: x-ray diffraction to confirm phase purity and crystal structure, Raman spectroscopy to study vibrational properties, and UV-Visible spectroscopy to calculate bandgap energy and Urbach energy. Before investigating any property of any material, it is essential to obtain a single phase of the material. Ordering of B site ions is a key player in affecting electronic and structure properties. In addition, the oxygen stoichiometry is influenced by synthesis routes. Hence, preparation of all compounds under investigation is done with extreme care to tailor the B-site ordering. In this section, the synthesis of Ga/Li co-doped NiO samples are discussed, along with the overview of fundamentals, experimental set-up used for characterizing samples. The working principle and necessary diagrams are provided.

Solid ion particles suspended in a colloidal solution (1 nm – 1 μm) in a solvent is called a sol. A gel is the formation of a semi-rigid mass when the solvent starts to evaporate from the sol and the particles/ions left behind; begin to connect with each other in a continuous regular chain.

Sol-gel is a chemical solution process for preparing powders, ceramics, and other materials. The sol-gel approach takes less time to process and yields a satisfactory result. When compared to the hydrothermal process, spray pyrolysis, and solid-state processes, it has higher control over stoichiometry, purity, and homogeneity. These strategies typically need a longer reaction time and more energy.

Sol evolves as an inorganic network containing a liquid phase which is known as a gel. Metal oxides are formed by joining the metals with oxo or hydroxy chains. As a result, metal-oxo or metal-hydroxy polymer solutions are formed. The gel is made up of dried to remove the liquid phase from it and finally forms a porous powder. After this, calcination

and annealing may be carried out. Generally, water-soluble for material synthesis, metal nitrates and metal acetates are used as precursors.

2.4 Synthesis of Ga/Li co-doped NiO: -

For the synthesis of nanocrystalline $\text{Ni}_{0.9844}(\text{Ga}_{1-x}\text{Li}_x)_{0.0156}\text{O}$ powders ($x=0, 0.25, 0.50, 0.75$ and 1), Nickel (II) nitrate, Lithium(I) nitrate and Gallium (III) nitrate, were added according to required stoichiometric ratio in separate beakers. All the precursors were soluble in DI water and hence a homogeneous solution was prepared after adding all the precursors and kept under magnetic stirring for few hours. Afterwards, gelling agents like citric acid and ethylene glycol was added in sufficient amount in each beaker. Then the resultant solution was moderately heated at $80\text{ }^\circ\text{C}$ on a hot plate till gel formation. It was then dried and heated further removing any trapped carbonate and nitrate phases and finally obtaining fluffy black powders containing nanoparticles of the prepared sample [Figure 2.3]. The black powder obtained was further annealed at $600\text{ }^\circ\text{C}$ in the muffle furnace [Figure 2.4] for decarbonisation and denitrification to take place and we obtain the required phase of our sample which is further confirmed by various characterization techniques.



Figure 2.4 Muffle Furnace used for annealing the prepared samples

2.5 Characterization Techniques: -

2.5.1 X-ray Diffraction (XRD): -

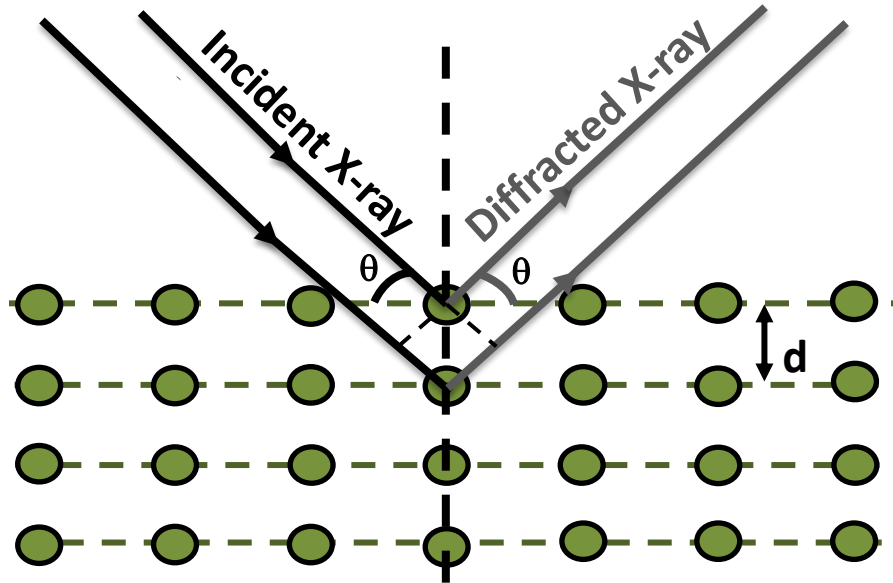


Figure 2.5 X-ray diffraction through Bragg's reflection in the atomic planes

Powder x-ray diffraction is a non-destructive technique for determining the structural properties of crystalline materials with long-range order. It has extensive applications in the realms of science, geology, medicine, the environment, and industry. The most common application of x-ray diffraction in crystallography is to determine the type and number of phases present in a chemical, unit cell dimensions and crystal structure, crystallite size, texture analysis, and residual strain based on their diffraction pattern[43]. Diffraction patterns are created when a monochromatic x-ray beam interacts with the electron cloud of the sample's atoms. Constructive interference occurs only when the path difference between diffracted rays is an integral multiple of wavelength of x-ray radiation [44].

The reflections of the lattice planes were used to identify the unknown structures. Crystals with high symmetry have a small number of atomic planes, whereas crystals with low symmetry have a larger number. X-rays have the wavelength of the order of 1 Å, which is the same as the interatomic spacing in the crystalline materials. Thus, the rays can interact with atoms and can reveal the atomic structure of the material obeying the Bragg's condition which can be given as: -

$$n\lambda = 2d\sin\theta \dots\dots\dots (2.1)$$

where n is the order of reflection (integer value i.e., 1, 2, 3...), λ is the wavelength of x-ray beam, d is the interplanar spacing between atoms, and θ is the angle between the incident and the reflected beam.

Working principle: -

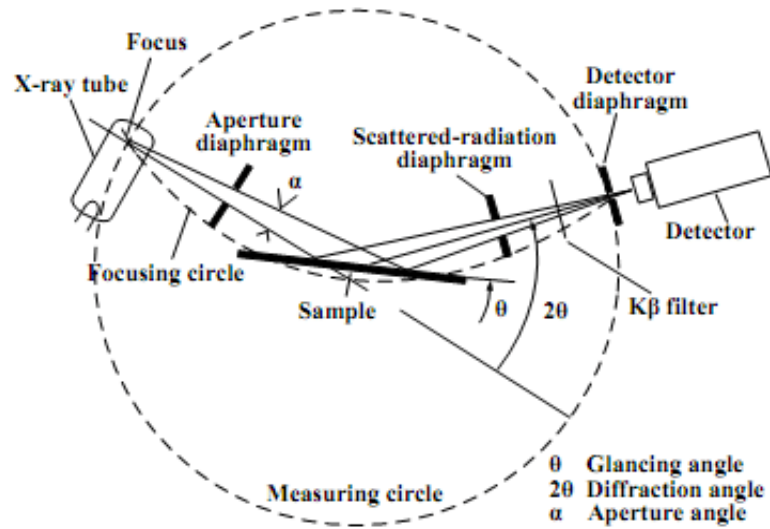


Figure 2.6 Schematic Diagram of a X-ray Diffractometer

The three main components of an X-ray diffractometer are the X-ray tube, sample holder, and detector [Figure 2.6]. They are very useful for acquiring diffraction peaks. The electrons produced by burning the filament in a CRT are then accelerated towards the target and bombarded to generate X-ray beam. When electrons have enough energy to remove electrons from the material's inner shells, they produce a characteristic X-ray spectrum. The most prevalent K and K components make up these

spectra. K now has two elements, K1 and K2 (K1 has a slightly shorter wavelength and is twice as intense as K2). The wavelengths are the target materials' characteristics (e.g., Cu, Fe etc.).

These photons are further filtered out using foils or crystal monochromators to produce a monochromatic X-ray. Because K1 and K2 have such similar wavelengths, the average of their wavelengths is used. Copper is the most common target material for Cu K radiation diffraction ($\lambda = 1.5418 \text{ \AA}$). These X-rays are collimated and targeted at the sample.

When x-rays collide with atoms in electronic clouds and constructive interference occurs, a typical powder pattern is obtained, which can be displayed as intensity vs 2θ . The powder patterns of the samples show peaks at specified values of 2θ that provide a distinctive 'fingerprint' that can be used to distinguish between crystalline and mixed phases.

Phase identification, purity, and structural modifications of all materials in this work were investigated using powder x-ray diffraction patterns recorded using a Bruker D2 Phaser X-ray diffractometer [Figure 2.7]. Diffraction patterns were obtained and were further compared with the CIF files from JCPDS data.

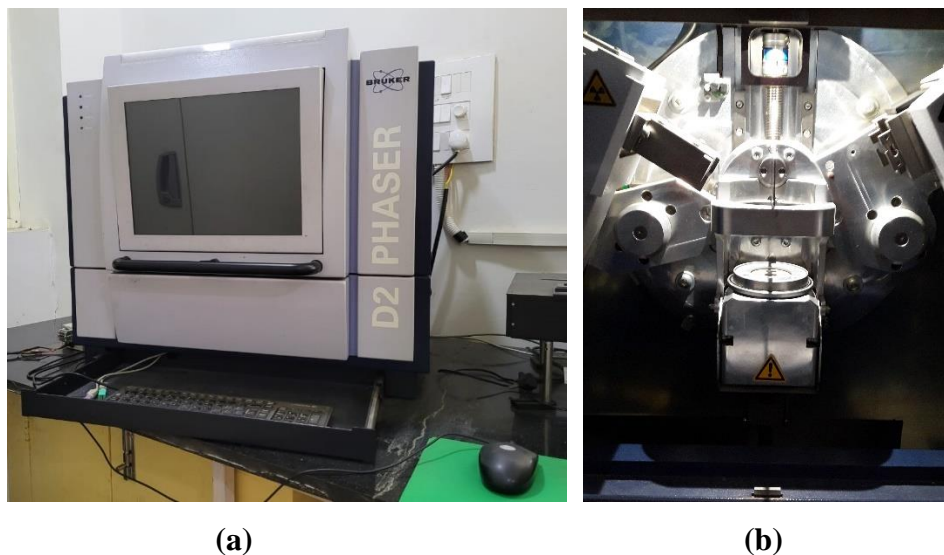


Figure 2.7 (a) Bruker D2 Phaser X-ray Diffractometer (b) Inside view of X-ray Diffractometer

Structural Analysis using Rietveld Refinement: -

Powder diffraction was once regarded to be useless in crystallography because of the apparent superposition of intensities, which limited structural information. As a result, the phase was determined purely by XRD. However, throughout time, a technique known as Rietveld refinement arose, which involves fitting the curve of the entire XRD diffraction data to extract the most information from the crystal structure. This method revolutionized the use of XRD for structural analysis [44]. This method was first developed for neutron powder diffraction data, and afterwards for X-ray powder diffraction data. This refinement method is a curve fitting method that considers several parameters (taking into account multiple parameters). The improved data output file provides crystal structure information (lattice parameters, atomic positions, displacement factors etc.) [43]. Furthermore, data such as crystallite size, intrinsic lattice strain, and crystallite phase fraction can be calculated, which is discussed in detail in the following chapter.

Rietveld refinement is often done using GSAS software [45]. This is the least-square fit method, which accounts for variables that affect diffraction peaks [46]. Individual reflection planes make up the observed diffraction pattern. Peak position, peak width, and peak intensity, all of which decline with distance, define each plane. The Rietveld method is very effective at refining powder diffraction data and extracting detailed structural information from the material. Although the Rietveld profile refinement is based on simple concepts, it does take some knowledge. Early refinement may diverge due to the presence of faulty beginning XRD data points and default instrument parameters. This method is just for structural refinement, not for structure determination. The suggested model is used to describe the crystal structure, experimental broadening, diffraction optics effects, and other sample factors (e.g., strain, anisotropy). The final crystallographic information files (.cif) can be utilized as an input file into the VESTA software to obtain the relative bond angles and bond lengths

of constituent elements in the compound after refining. The following are the system requirements:

Model: Bruker D2 Phaser x-ray diffractometer, Max Power: 3 kW

X-ray target: Cu anode ($K\alpha = 1.5406 \text{ \AA}$), Operating voltage: 30 kV

Optics: Bragg Brentano, Parallel beam

2.5.2 Raman Spectroscopy: -

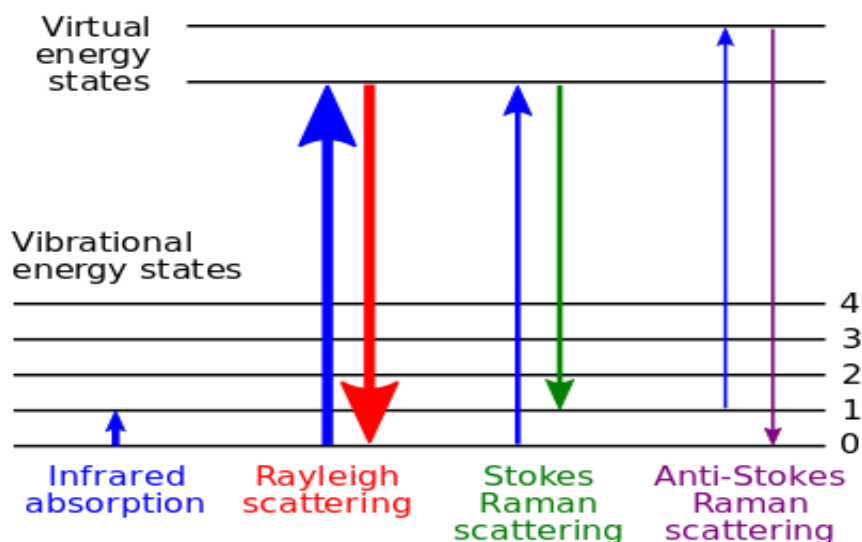


Figure 2.8 Schematic diagram showing Raman scattering

Vibrational transitions can be seen in both infrared and Raman spectra. These are highly sensitive instruments for studying crystal lattice structure. The data obtained using mercury discharge lamps as monochromatic sources and photographic film as detectors was deemed a watershed moment. In 1942, photoelectric detectors were invented, and in 1966, lasers were used as an excitation source in Raman spectroscopy [47].

The most powerful technique in material science is vibrational spectroscopy. It involves the scattering of electromagnetic radiation by atoms or molecules and may offer qualitative and quantitative structural information for a variety of compounds in a variety of states. The obtained spectrum gives information about the structure and behavior of the solid

substance. This technique is commonly used to examine many types of modes in the low and high frequency ranges, such as vibrational and rotational modes [48]. When a sample is irradiated with a monochromatic light source using a spectrometer, this technique produces inelastic Raman scattering. Most photons are scattered with the same frequency as the incident laser light when a material is bombarded by a high-intensity monochromatic light source, such as a laser. This elastically scattering mechanism is known as Rayleigh scattering[49]. However, certain photons, about one out of every ten million, have an energy shift when compared to the initial laser energy. Raman scattering is a mechanism that occurs when lower or higher energy scattering occurs. Stokes scattering is produced by Raman scattering of atomic vibrations starting from the ground vibrational state. Anti-Stokes scattering occurs when a photon interacts with a phonon in a vibrationally excited state, which can be illustrated using a quantum energy diagram [Figure 2.8]. The intensity of photons in relation to each energy difference is directly linked to chemical bonds and hence a Raman spectrum can be obtained. Figure 2.9 depicts a schematic view of a Raman spectrometer.

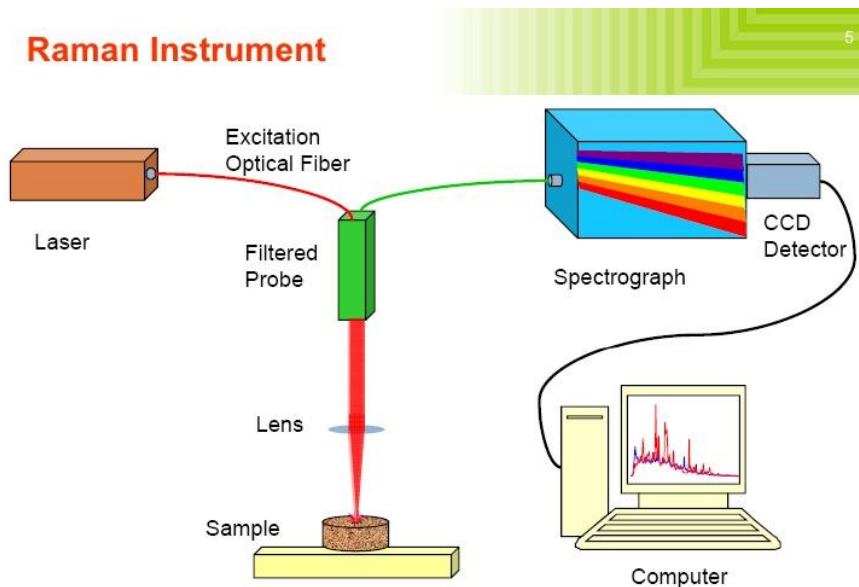


Figure 2.9 Schematic representation of Raman spectrometer

A Raman spectrometer's essential components are as follows:

(i) **Excitation source (Laser)**: A good laser should have a short linewidth and an exceptionally stable output.

(ii) **Light collection optics and sample illumination system**: Normally, a laser beam (UV, Visible, or NIR) is shone on the sample, the scattered rays are collected with a lens, and the sample's Raman profile is obtained by passing it through a spectrophotometer.

(iii) **Wavelength selector (Filter or Spectrophotometer)** is used to separate the incident light spatially according to the wavelength.

(iv) **Photodiode array, CCD, or PMT detector**: Detector is a key component of the Raman spectrometer. Depending on the excitation laser used, a variety of detectors are available. For visible excitation, a typical CCD is employed, for UV excitation, a photomultiplier tube (PMT), and for NIR excitation, an indium gallium arsenide (InGaAs) array is ideally suited[50]. The materials were analyzed using a micro-Raman system from Jobin Yvon Horiba LABRAM- HR visible spectrometer. The room temperature Raman spectra of all samples $[\text{Ni}_{0.9844}(\text{Ga}_{1-x}\text{Li}_x)_{0.0156}\text{O}]$ powders ($x=0, 0.25, 0.50, 0.75$ and 1) were measured using a laser beam of 633 nm excitation wavelength.

2.5.3 Ultraviolet–Visible Absorption Spectroscopy: -

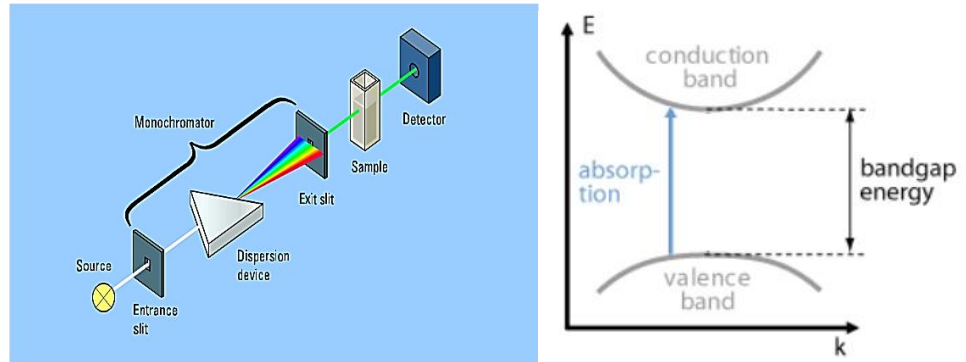


Figure 2.10 (a) Schematic representation of UV-Visible Spectrophotometer (b) Schematic diagram of bands in solids

The absorption of visible and ultraviolet light occurs when electrons are excited from a lower energy level to a higher energy level in atoms or molecules. Because all atoms and molecules have quantized energy levels, only light with the exact quantity of energy may produce a transition and be absorbed. As a result, the molecule must have a bond or atoms with non-bonding orbitals to absorb light in the spectroscopic range 200-800 nm (lone pair of electrons). Various physical phenomena such as reflectance, absorbance, scattering, and fluorescence are observed when electromagnetic radiation is illuminated on material. UV-Visible (UV-Vis) spectroscopy investigates how UV-Visible light interacts with the specimen. When a sample absorbs light of a specific wavelength, an electron moves from the filled orbital to the unoccupied or partially filled orbital. The energy bandgap is revealed by this constant wavelength of light.

The absorption of a material at a given wavelength is defined using Beer-Lambert law [51] as:

$$A = -\log (I/I_0) \dots\dots\dots (2.2)$$

where I and I₀ are the intensities of the radiation incident and transmitted through the sample. The amount of absorption (A) is proportional to the number of absorbing species(c) present and the distance travelled by the

light through the sample (l). On summarizing the above factors, absorbance can be given as

$$A = \epsilon \cdot c \cdot l \dots\dots\dots (2.3)$$

where ϵ is the molar absorption coefficient (extinction coefficient) of the sample.

Kubelka-Munk function[52], F(R) represented in the equation can be written in terms of absorption,

$$F(R) \propto \alpha \propto (h\nu - E_g)^n / h\nu \dots\dots\dots (2.4) \quad \text{or,}$$

$$(F(R)h\nu)^{1/n} = (\alpha h\nu)^{1/n} = A (h\nu - E_g) \dots\dots\dots (2.5)$$

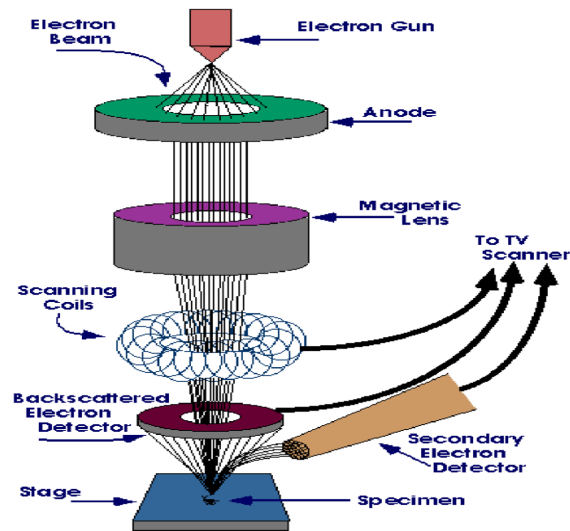
where A is a constant independent of the photon energy, α is the absorption coefficient, $h\nu$ is incident photon energy, E_g is the band gap energy and n is a constant. For direct bandgap, $n=1/2$ and for indirect bandgap, $n=2$. For both examples, the band gaps from $(\alpha h\nu)^{1/n}$ vs $h\nu$ plots were calculated using the intercepts of the extrapolated linear sections of the equations. At room temperature, optical absorption in the range 200–800 nm was examined using a Research India UV–Vis spectrophotometer [Figure 2.11] The Tauc plots were created from the reflectivity data using the Kubelka-Munk approach [53], [54].



Figure 2.11 Experimental Set-up for UV-Visible Spectrophotometer

2.5.4 Field emission scanning electron microscopy

(FESEM): -



(a)



(b)

Figure 2.12 (a) Schematic Diagram of Field Emission Scanning Electron Microscope (b) #1 Complete arrangement of the FESEM. #2 Connected computer systems running user-friendly software. #3 EDX measurement system. #4 It is a complete set of gold sputtering. #5 Enlarged part of the sample holder of the gold sputtering system.

The FE-SEM (Field emission scanning electron microscopy) utilizes a low energy electron beam from a field emission gun to produce the surface

image of the sample. This method is particularly effective for measuring sensitive samples that have a low melting temperature, such as ceramics. On such samples, standard scanning electron microscopy is unable to offer trustworthy information. An optical microscope is based on light diffraction and has a spatial resolution of a few micrometres. To picture things on the nanometre scale, better resolution in the range of a few nm is required, which necessitates the use of light with a wavelength in nm. When compared to visible light, the narrow electron beam spot provides significantly superior spatial resolution. The FESEM produces better, less distorted images with a spatial resolution of 1 nm, which is superior to optical microscopy and scanning electron microscopy. Auger electrons, secondary electrons (SEs), backscattered electrons (BSEs), and X-rays were created when the energetic electron collided with the materials. For image construction, FESEM uses SEs and BSEs, and x-rays for elemental/composition analysis [Figure 2.12 (a)].

Secondary electrons (surface morphology): Secondary electrons are utilized to image the surface of the materials. These are from the sample's near-surface regions (less than 10 nm). The inelastic collision between the energetically primary electron and the material is the mechanism that generates these electrons. Secondary electrons are excellent for analysing the surface morphology of a sample.

Back-scattered electrons: A vast portion of the interaction volume creates back-scattered electrons. Back-scattered electrons are produced during elastic collisions of electrons and atoms. This causes the electrons' route to alter. This event is described by the "billiard-ball" model, in which small particles (electrons) collide with larger particles (atoms). The number of backscattered electrons that reach the detector is proportional to their 'Z' number, allowing for phase separation. It creates visuals that convey information about the sample's composition.

Energy-dispersive X-ray spectroscopy:

The elemental analyses were investigated using the energy dispersive X-ray spectroscopy (EDS, EDX, and EDXS) technique. It can determine the relative amount of each element and map the element's distribution. FESEM includes an EDX component. The X-ray is generated in two steps in FESEM.

First step: When an electron beam collides with a sample, the energy is transferred to the atoms in the sample. Electrons may be knocked off the atom or jump to a higher energy shell as a result. This transition results in the formation of holes.

Second step: Higher energy shell electrons recombine with lower energy shell holes. X-rays were generated as a result of the energy difference between these two shells. Each element's atomic number and a unique characteristic are linked to the generated x-ray. The elements are identified using the energy of these transitions.

FESEM micrographs were taken on the pellet surfaces of the samples in this study. These photos were captured with a Supra55 Carl Zeiss FESEM [Figure 2.12 (b)]. The charging effect is noticeable because ZnTiO₃-based materials are very insulating/nonconductive. As a result, a metallic gold deposition (5 nm) by sputtering techniques was necessary for charge drainage from the surface to avoid the charging effect.

System specifications:

Make: Zeiss Model: Supra 55

Operating voltage: 0.02–30 kV Working distance: up to 100 nA Variable pressure mode: up to 133 Pa

Chapter 3

Results and Discussion

3.1 Structural, Optoelectronic and Electrical Studies of NiO nanostructures

3.1.1 X-Ray Diffraction (XRD)

From the X-ray diffraction studies it is confirmed that NiO single cubic phase has been successfully formed having space group $Fm\bar{3}m$. The differences in the XRD patterns of the three samples are minor because their chemical and physical properties are similar. Furthermore, all of the samples exhibit characteristic peaks of diffraction pattern at $2\theta = 37.29^\circ$, 43.54° , and 62.94° , 75.61° and 79.62° , which correspond to the (111), (200), (220), (311) and (222) of the face-centered cubic unit cell, respectively, with lattice constant of roughly 4.18 \AA [Figure 3.1 (a)]. The highest peak of intensity profile is at (200), followed by peaks at (111) and (220). The average crystallite sizes were 18.29, 12.62 and 27.52 nm for nanosheets (C1), microspheres (C2) and flake-flowers (C3), respectively as derived using Scherrer equation [Figure 3.1 (b)]. Rietveld refinement of the samples were also done [Figure 3.2] and the variation in bond length, bond angle and lattice parameters were found out as shown in the figure given below [Figure 3.1]. Although all the samples are comprised of pure NiO yet it can be seen that there is a considerable change in the bond lengths and lattice parameters which can be attributed to the change in morphology and shape of the different nanostructures obtained through hydrothermal treatment [Figure 3.1 (c-e)].

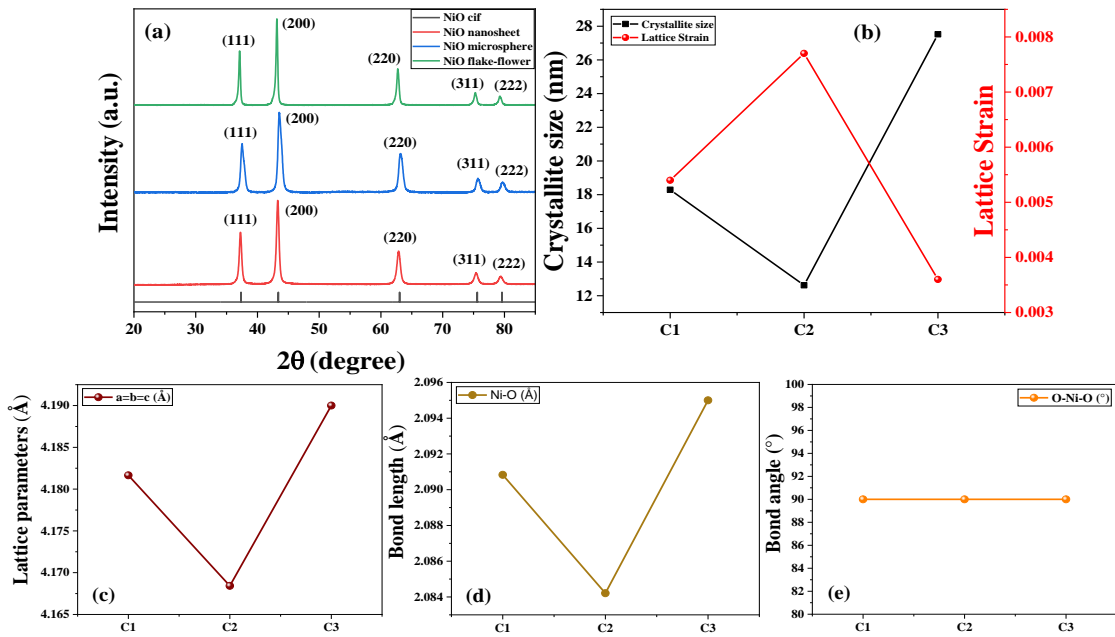


Figure 3.1 (a) X-ray Diffraction Patterns of NiO nanostructures (C1-nanosheet, C2-microsphere, C3-flake-flower) (b) Variation of Crystallite size and Lattice Strain (c) Variation of lattice parameters (d) Variation in bond length (e) Variation in bond angle

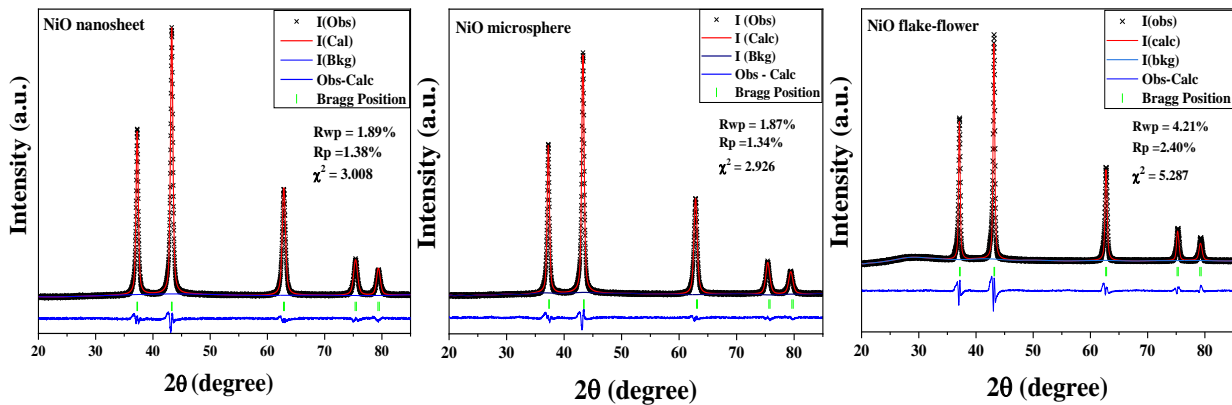


Figure 3.2 Rietveld refinement plot of the NiO nanostructures

3.1.2 Raman Spectroscopy

From the room temperature Raman spectra of the prepared nanostructures, it can be observed that there is one prominent peak at 500 cm^{-1} which is the 1LO mode [55] and two broader and less intense peaks at 410 cm^{-1} and 1050 cm^{-1} which are recognised as 1TO and 2LO mode respectively [55]. Although all the samples are comprised of pure NiO, it can be readily seen

that the intensity of the Raman modes are varying for the three samples. This modification may be due to the change in morphology and particle shape and size of the samples. The 1LO mode arises due to O-O planar vibrations and conversely 1TO mode arises due to O-O transverse vibrations perpendicular to the lattice plane [55]. A 2LO mode is also observed which is much broader and less intense than the other peaks which can be attributed to the Ni-O stretching vibrations [55] [Figure 3.3].

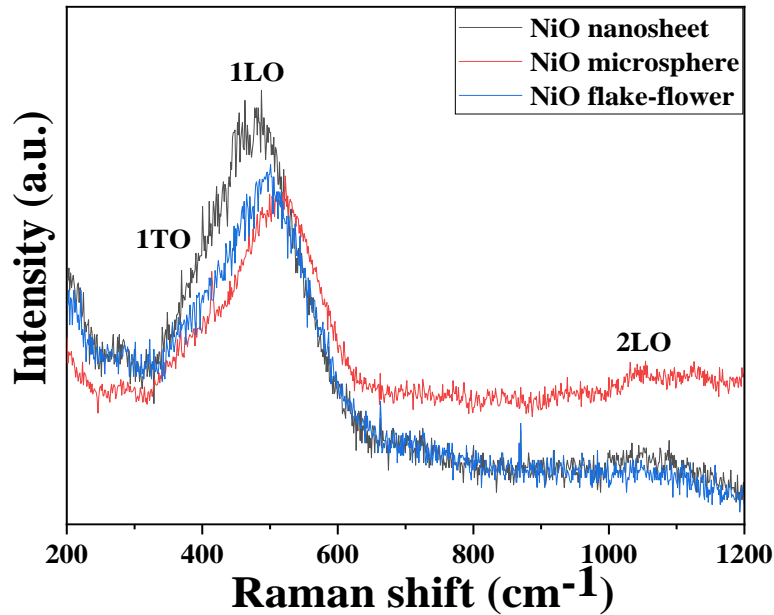


Figure 3.3 The room temperature Raman spectra of NiO nanostructures annealed at 450 °C.

3.1.3 UV-Visible Spectroscopy

UV-Visible spectroscopy refers to absorption spectroscopy or reflectance spectroscopy. UV-visible radiation region ranges from 100 nm to 800 nm. Light of this wavelength is able to affect the excitation of electrons in the atomic or molecular ground state to higher energy levels giving rise to the absorbance at wavelengths specific to each molecule. It is the measurement of attenuation of a beam of light after it passes through a sample or after reflection from a sample. UV-vis spectroscopy is especially significant in the determination of electronic bandgap (E_g) and lattice disorder (Urbach energy, E_u).

Band gap was evaluated from the Diffuse Reflectance Spectroscopy using Kubelka Munk Theory. At room temperature, the fluctuation in reflectance, R , with changing wavelength was recorded. $A+T+R=1$, where the material's absorbance and transmittance are A and T respectively. As a result, $1-R$ equals $A+T$. T approaches to zero for very thick samples and translucent materials. As a result, $1-R$ equals A . $(1-R)^2$ is the intensity owing to A . The absorption coefficient ' α ', is determined by the material's scattering capability in addition to its absorption capability. The capability of scattering is proportional to R and is equal to $2R$. The lower the absorption coefficient, the bigger the scattering. As a result, one may express α as a "Kubelka-Munk" function where $\alpha = F(R) = (1-R)^2/2R$, by combining these two contributions. A plot of $F(R)$ versus $h\nu$ can be plotted. However, such an analysis requires a further modification with regards to the nature of the materials band gap. A so-called Tauc plot was plotted of $(F(R)h\nu)^{1/n}$ versus $h\nu$, where, $n=0.5$ for direct band gap while $n=2$ for indirect bandgap. In a direct band gap semiconductor, momentum vector of the highest energy of the valence band coincides with the momentum vector of the lowest energy of the conduction band. In an indirect band gap semiconductor, these two momenta are different.

The band gap can be calculated from the linear portion of the Tauc plot using the ratio of the intercept and the slope, $E_g = (-\text{intercept})/(\text{slope})$.

For the direct band gap, E_g is calculated to be ~ 3.54 eV for C1, ~ 3.47 eV for C2 and ~ 3.56 eV for C3 samples. These changes in band gap are very nominal and can be attributed only to the changes in morphology in the samples. Also, there is a variation in the Urbach energy which gives an idea about the lattice disorder. It is observed that the Urbach energy is highest for C2 (~ 314.26 meV), lowest for C3 (~ 150.87 meV) and intermediate for C1 (~ 235.52 meV). From this it can be concluded that for sample C2, lattice disorder is maximum and minimum in case of C3.

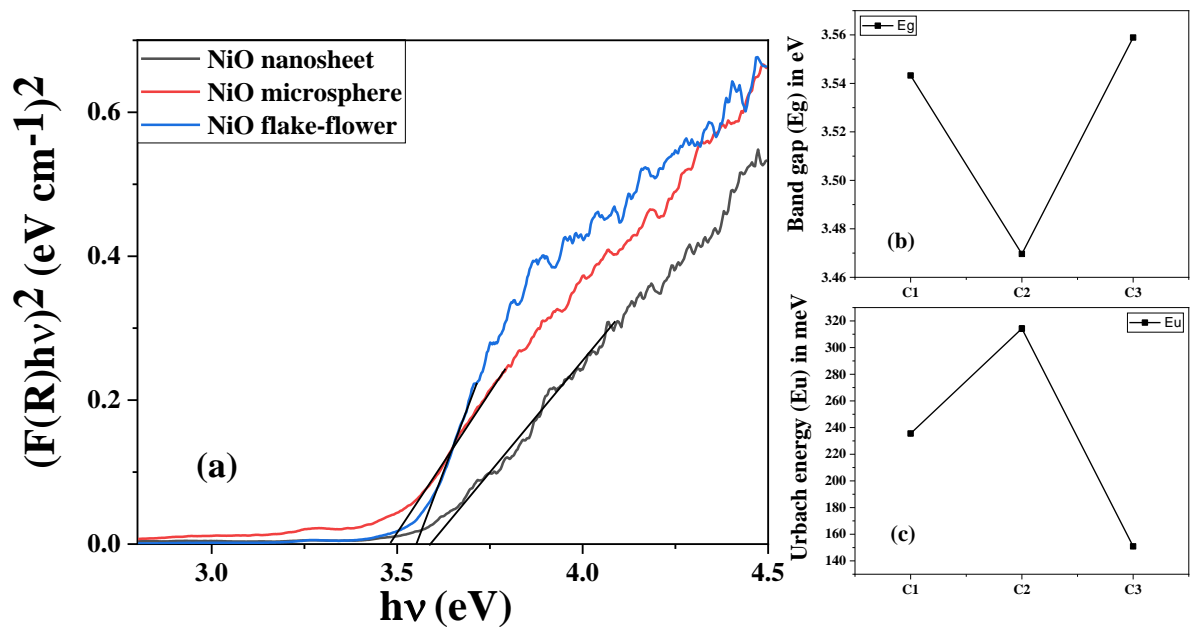


Figure 3.4 (a) Absorption spectra of UV-Vis for NiO nanostructures (C1-nanosheet, C2-microsphere, C3-flake-flower) (b) Variation in the band gap energy (c) Variation in the Urbach energy.

3.1.4 FESEM and EDX Data Analysis: -

The SEM images for NiO nanostructures are shown in Figure. The micrographs show a uniform distribution of grains all through the samples. High quality FESEM images of samples C1, C2 and C3 were observed [Figure 3.5 (a-c)]. The FESEM study was performed to investigate the particle size and morphology of all samples. Highly agglomerated particles were observed. ImageJ software was used to calculate the actual particle sizes of C1, C2 and C3. For sample C1, nanosheets of ~100-110 nm was observed. For sample C2, microspheres of ~60-80 nm were observed. For sample C3, flake-flower structures of ~90-100 nm were observed.

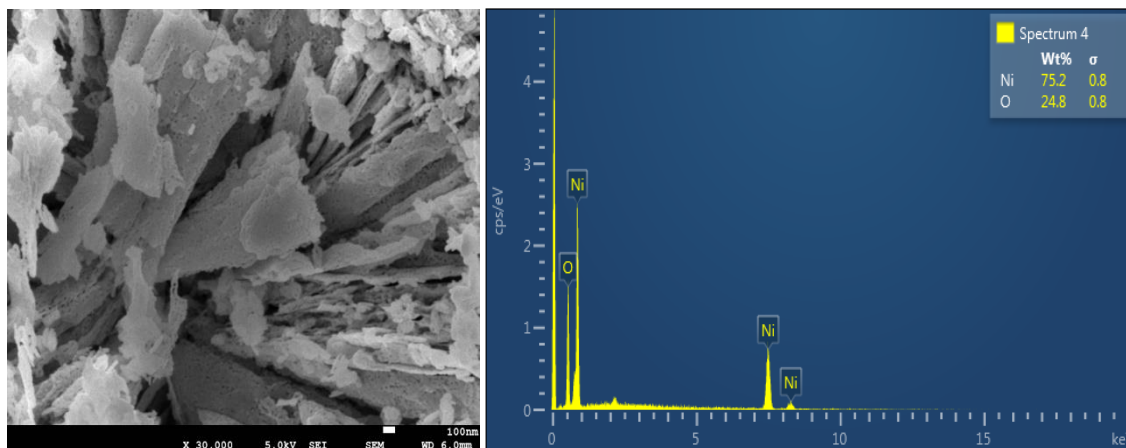


Figure 3.5 (a) FESEM and EDX Data of NiO nanosheet (C1)

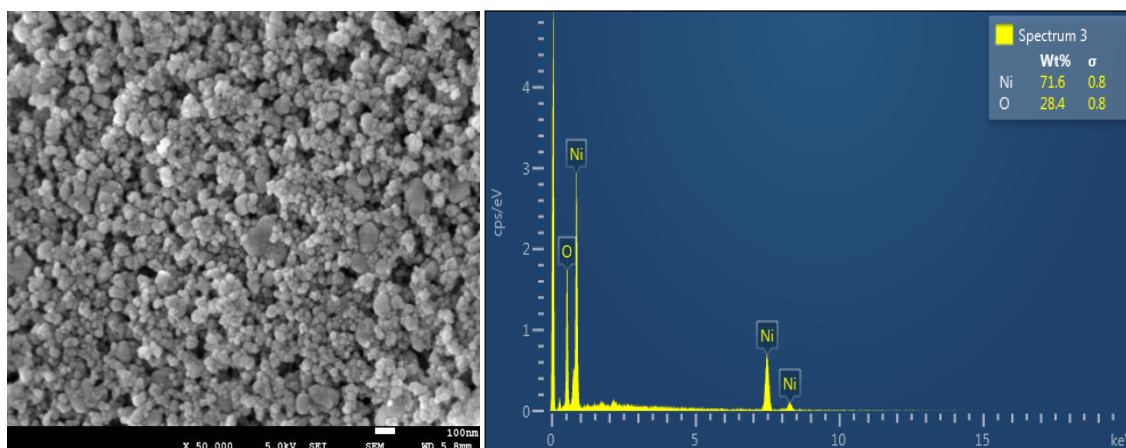


Figure 3.5 (b) FESEM and EDX Data of NiO microsphere (C2)

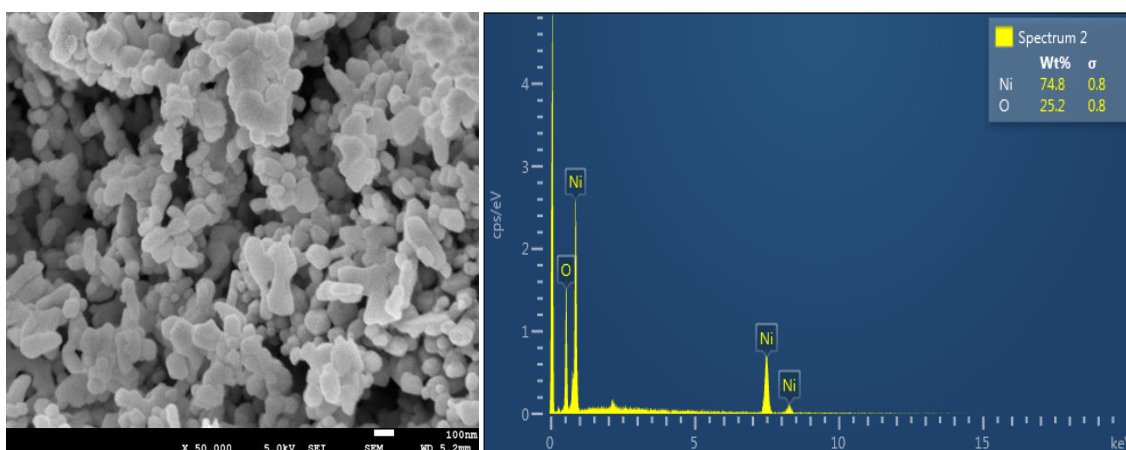


Figure 3.5 (c) FESEM and EDX Data of NiO flake-flower (C3)

3.2 Structural, Optoelectronic and Electrical Studies of Ga/Li co-doped NiO

Nickel oxide (NiO) has a cubic lattice structure similar to NaCl or rock salt structure with Ni^{2+} and O^{2-} ions as octahedral sites i.e., Ni atoms form octahedra with six O atoms [5]. In this structure, nickel atoms occupy the corners of the cube and the centers of the faces, while oxygen atoms occupy the centers of the edges and the center of the cube, following the characteristic fcc-packed structure and having a space group $Fm\bar{3}m$ [5]. Ni $3d^8$ and O $2p^6$ have similar energy levels. As a result, a substantial electronic hybridization is feasible, allowing for a bandgap of 3.4 to 4 eV in the material [7]. Stoichiometric NiO itself shows insulating behaviour. The low conductivity of stoichiometric NiO prevents electron-hole recombination, which results in reduced hole transport. Ni-vacancies, on the other hand, can cause inherent p-type conductivity. Oxygen vacancies are also linked to such molecules. Ni-vacancies, on the other hand, have been explored in both O-rich and O-deficient situations. For oxygen-rich conditions, the formation energy is low, while for oxygen-deficient conditions, it is high. The conduction mechanism can be conventionally expressed in terms of the band or can be interpreted in terms of small polaron hopping (SPH). Polarons develop in SPH as a result of strong interactions between the lattice and carriers. NiO has a very broad bandgap and has attracted attention because to its improved hole mobility and stability, but the difficulty is that it has a weak built-in field strength. Because of its deep valence band edge (from -5.3 eV to -5.4 eV), lithium doping can improve hole extraction and increase open-circuit voltage. However, to the best of our knowledge, the effect of Li inclusion on the bandgap of Gallium doped NiO synthesized by sol-gel has not been thoroughly explored. The structural, optical, electrical, and morphological characteristics of Ga and Li doped NiO processed by sol-gel were investigated in this study [56]. The findings show a substantial relationship between structural defect states, bandgap modulation and

conductivity in NiO. The feasibility of employing nanoparticle NiO is due to its easy synthesis: the synthetic strategy plays a crucial role in modifying the NiO structure. Furthermore, a synergistic effect of the cubic NiO with the Lithium incorporation can amplify the former's performances, produced by the sol-gel process. It has altered the defects and has greatly reduced the bandgap with the rapid tuning of the interstitial and the vacancy defects. The Li, in combination with the NiO semiconductor, forms deep level transportation of electrons and helping in scavenging the holes for quick transformation and recombination. Moreover, Li doping results in shifting of the conduction band towards the positive direction narrowing the bandgap. Despite such benefits, there are few reports investigating the impact of the Li dopant with the enhanced bandgap tuning and its relationship with the defects.

3.2.1 X-Ray Diffraction Analysis:-

All the Ga/Li doped samples [$\text{Ni}_{0.9844}(\text{Ga}_{1-x}\text{Li}_x)_{0.0156}\text{O}$] were annealed at 600°C where $x=0, 0.25, 0.50, 0.75$ and 1.0 are represented by S1, S2, S3, S4 and S5 respectively and pure NiO by S0. The cubic structure of NiO having space group ($\text{Fm}\bar{3}\text{m}$) is confirmed by Rietveld refinement of the X-ray Diffraction (XRD) patterns obtained for all the samples. No extra phases other than *NiO* are observed related to any complex mixed oxides of *Li* and *Ga* [Figure 3.6 (a)]. Rietveld analysis was performed using GSAS software. Acceptable goodness of fit (χ^2) values was obtained for all the samples. The analysis confirms the *NiO* ($\text{Fm}\bar{3}\text{m}$) phase [Figure 3.7]. Lattice parameters ($a=b=c$) was initially same ~ 4.16843 Å for S0 and S1, but decreased to 4.16841 Å in S2, increased to 4.16845 Å in S3 but again reduced to 4.16843 for S4. Only a nominal change in the lattice constants were observed for all samples [Figure 3.6 (c)]. NiO₆ octahedra are formed by octahedrally bonded Ni and O atoms. In the VI coordination state, the ionic radius of the host Ni²⁺ (0.69 Å) is larger than Ga³⁺ (0.62 Å), but smaller than Li⁺ (0.76 Å). Extra oxygen may be added

into samples S1, S2, and S3 to maintain charge balance in the lattice due to Ga^{3+} having larger cationic charge than the host Ni^{2+} . This may create oxygen interstitials, which could lead to lattice expansion. However, because Li^+ has a lower charge (+1) than Ni^{2+} , the amount of oxygen vacancy in the exclusively Li^+ doped sample can be enhanced. As a result, the gradual decrease in the lattice strain can be linked to the elimination of oxygen from the lattice. The bond length decreases for samples S0, S1, S2 and increases for sample S3 [figure 3.6(d)]. As predicted, a similar trend of variation was also observed in lattice constants and bond lengths. Strain is linked to lattice disorder, and so to long-range order. A less strained lattice is observed to have larger crystallite sizes and shorter bond lengths, and vice versa [57]. The Williamson Hall-method and the Scherer equation were used to estimate strain and crystallite size, with the help of Tiny tools software. For samples S0 to S1, the crystallite size decreased and thereafter increased for samples S2, S3 and S4 while the lattice strain increased for samples S0 to S1, and decreased for samples S2, S3 and S4 which is quite obvious from the trend in crystallite size [Figure 3.6 (a)]. The host Ni^{2+} (VI) [0.69 Å] is larger than Ga^{3+} (VI) ion [~0.62 Å] but smaller than Li^+ (VI) [~ 0.76 Å]. For S1 a smaller but higher charged Ga^{3+} ion is incorporated in the lattice. This will invite more oxygen in the lattice thereby at first neutralizing the latent Vo and thereby introducing Oi . This will create a positive pressure on the lattice, thereby increasing the bond lengths and thereby the lattice parameters. This is what was observed from the Rietveld refinement. For S2 the trend continues due to the presence of Ga^{3+} ion, but the presence of Li^+ ion somewhat compensates for the extra charge. At the same time, the Li^+ ion is larger than the Ni^{2+} ion which continues to exert the positive pressure on the lattice. However, the effect is somewhat reduced by the loss of oxygen due to the lesser charge of the Li^+ ion. In the S3 sample, increasing the Li^+ concentration should cause the lattice to expand on the one hand, but due to its lower charge than the parent Ni^{2+} , Vo will be generated in the lattice, forcing the lattice to

contract. The lattice strain and crystallite size increased and reduced accordingly and was logical to the analysis of charge and size of the dopants.

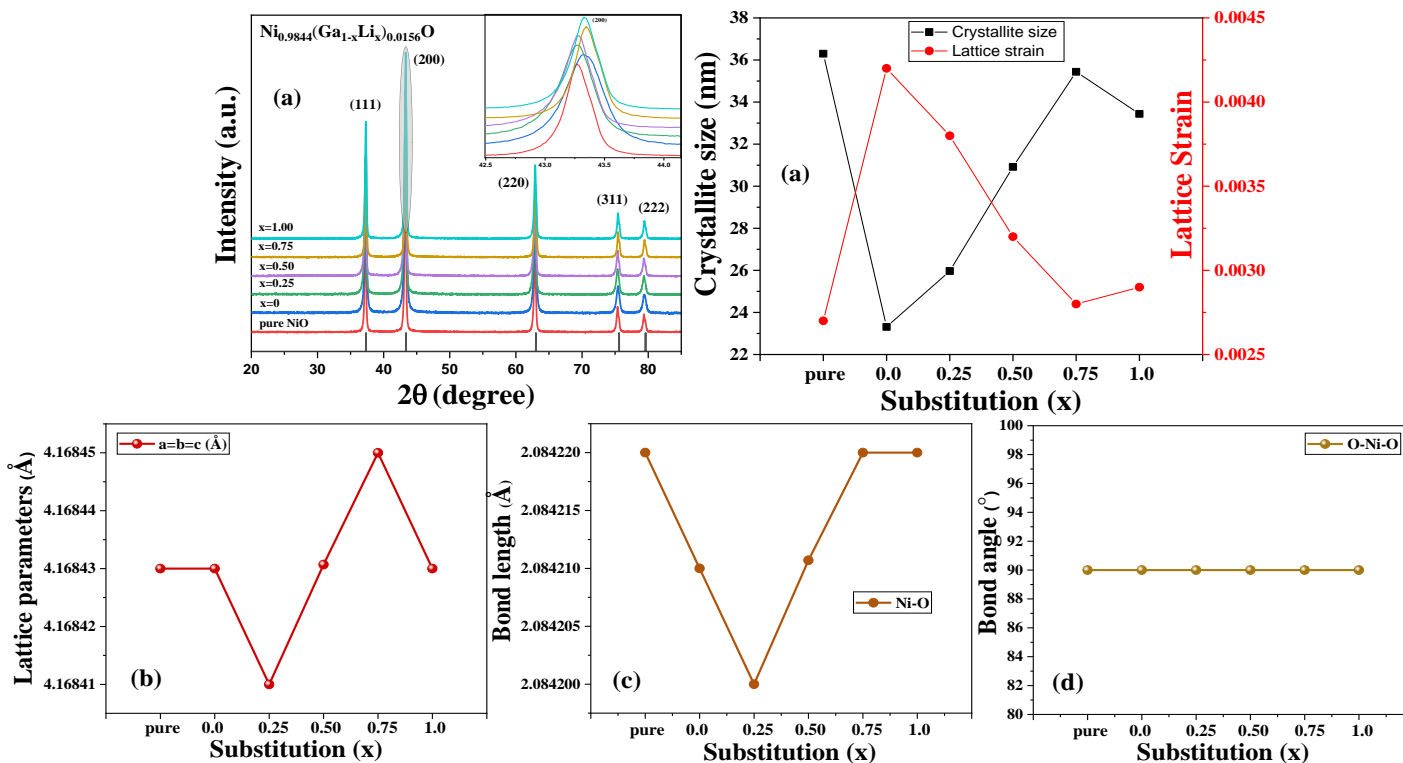


Figure 3.6 (a) XRD Pattern of $\text{Ni}_{0.9844}(\text{Ga}_{1-x}\text{Li}_x)_{0.0156}\text{O}$ for $x=0, 0.25, 0.5, 0.75$ and 1 (b) Variation of Crystallite size and Lattice Strain (c) Variation of lattice parameters (d) Variation in bond length (e) Variation in bond angle.

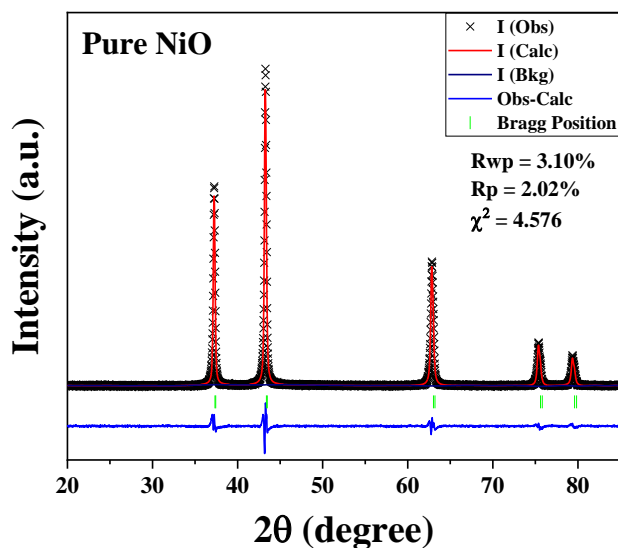


Figure 3.7 Rietveld refinement of pure NiO from the above series $\text{Ni}_{0.9844}(\text{Ga}_{1-x}\text{Li}_x)_{0.0156}\text{O}$ Annealed at 600°C

3.2.2 Raman Spectroscopy: -

Raman spectroscopy is a powerful tool for studying lattice vibrations and structural information at the scale of a few lattice constants. The room temperature Raman spectra of the Ga/Li doped NiO samples are shown in Figure 3.8 Raman spectra of S0 reveals one prominent mode at 501.8 cm^{-1} along with two less intense modes at 496 cm^{-1} and 1090 cm^{-1} . These three modes have been identified in literature as 1LO, 1TO and 2LO modes, respectively [55]. The O–O planar vibrations known as longitudinal optical one phonon-mode (1LO) produce the band at 501.8 cm^{-1} . This mode blue shifts to higher frequencies for doped materials, reaching 511.47 cm^{-1} for S1 and 514.52 cm^{-1} for S2, before red shifting to 506.02 cm^{-1} for S3 and 500.44 cm^{-1} for S4, but only slightly blue shifting to 500.77 cm^{-1} for S5, which is considered insignificant [Figure 3.9 (a)]. This mode is caused only by an O-O planar vibration and does not involve cation vibration. In S0, the 1TO mode is seen as a prominent peak at 389.8 cm^{-1} . This mode blue shifts to 399.5 cm^{-1} in S1, 402.6 cm^{-1} in S2 and 406.6 cm^{-1} in S3 followed by a red shift to 386.2 cm^{-1} in S4 and 378.9 cm^{-1} in S5. [Figure 3.9 (b)]. This mode shows the amount of Vo's in the lattice effectively. The Ni–O stretching vibrations known as two-phonon scattering produce the band at 1090 cm^{-1} (2LO). A 2LO mode is generally reported in the literature and is sometimes extremely prominent. This mode red shifts continually from 1089 cm^{-1} in S0, to 1088 cm^{-1} in S1, 1068.4 cm^{-1} in S2, 1059.6 cm^{-1} in S3, 1019.8 cm^{-1} in S4 and 955.3 cm^{-1} in S5 [Figure 3.9 (c)]. In these samples the 2LO mode seems to become less intense with the increasing Li^+ content. This may be due to the decrease in strain in the Li-rich samples leading to larger crystallite sizes. Since phonon frequency is proportional to the square root of bond strength and inversely proportional to the square root of the effective masses of the vibrating atoms, such changes are most likely to affect the phonon modes of the co-doped samples in terms of frequency and intensity.

The increase in FWHM values for 2LO mode at 1090 cm^{-1} indicates an increase in surface defects, resulting in a drop in crystallite size and an increase in lattice strain. The FWHM increase for sample S1, S2 and decrease for S3 hints the decrease of lattice strain and hence defects [Figure 3.9 (f)]. Because of the larger cationic charge-imbalance caused by the introduction of Li and Ga, the defects first increase and then reduce for S3. In XRD data, a similar trend of variation of lattice constants and lattice strain was observed. It means that when Li^+ ions were introduced into the sample, the lattice shrunk, reducing defects like O_i 's and creating more V_o 's.

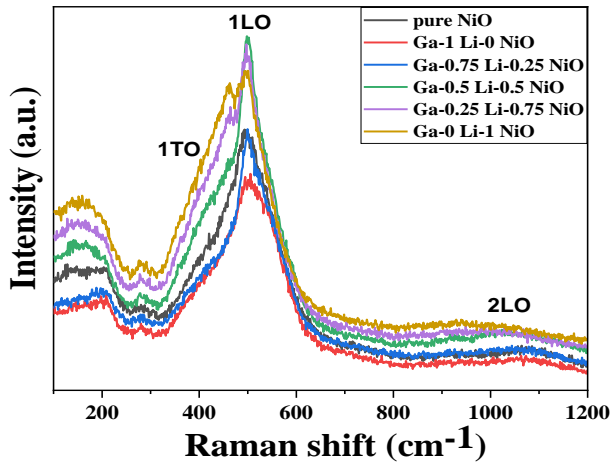


Figure 3.8 Raman Spectra of $\text{Ni}_{0.9844}(\text{Ga}_{1-x}\text{Li}_x)_{0.0156}\text{O}$ annealed at 600 °C

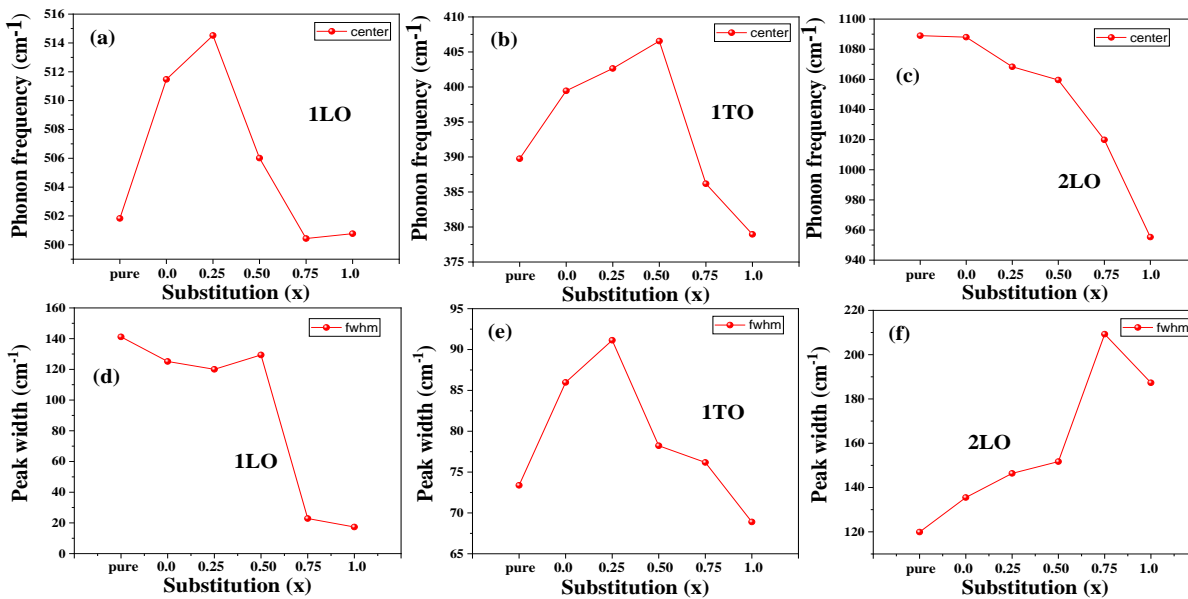


Figure 3.9 Variation in the phonon frequency and peak width with different doping concentrations of $\text{Ni}_{0.9844}(\text{Ga}_{1-x}\text{Li}_x)_{0.0156}\text{O}$

3.2.3 UV-Visible Spectroscopy Analysis: -

DRS measurements (UV-Vis Spectroscopy) were performed and the percentage reflectance, %R, was recorded in the area (200-1100 nm) to estimate the band gap, E_g , of the materials experimentally [Figure 3.10 (a)]. To eliminate the probability of transmission, thick samples were used. This eliminates all other possibilities, leaving simply absorbance and reflectance. In extremely opaque materials, the Kubelka-Munk function[52] is used to calculate the equivalent absorption coefficient, $F(R) = (1-R)^2/2R$, where R is the diffuse reflectivity of the samples. The diffuse reflectivity increases dramatically at the band boundary. In this area, there is a linear zone with an unusually steep slope. The absorption coefficient decreases exponentially in this region. The beginning of this exponential decline is often regarded as a universal method for detecting absorption edges from which the bandgap may be calculated. The absorption edge was calculated using a linear fit to R's linear portion. Using the Tauc method [54], the optical band gap was computed using energy-dependent optical absorbance data. $(\alpha hv)^{1/n} = A(hv - E_g)$; where α is the absorption coefficient, hv is the photon's frequency, h is Planck's constant, A is a proportionality constant, and E_g is the band gap. The nature of the transition between the conduction band (CB) and the valence band (VB) is determined by the power coefficient n , which is 1/2, 3/2, 2, and 3 for direct allowed, direct prohibited, indirect allowed, and indirect forbidden transitions, respectively.

The E_g was calculated using $n=1/2$ (for direct E_g) and 2 (for indirect E_g). For the direct band gap, only a minor increase of E_g can be observed in S1 (~3.578 eV) and S2 (~3.581 eV) with solely Ga^{3+} doping compared to S0 (~3.526 eV). The E_g value of S3 (~3.526 eV) is identical to that of S0. Thereafter, E_g drops significantly in S4 (~3.458 eV) and even more so in S5 (~3.396 eV) [Figure 3.10 (b)]. This obviously demonstrates Vo's importance in the system. An indirect band gap estimate, on the other hand, yielded values of 3.248 eV for S0, 3.34 eV for S1, 3.392 eV for S2,

3.256 eV for S3, 3.094 eV for S4, and 2.804 eV for S5 [Figure 3.10 (d)]. As the Li^+ content rises, the lattice becomes more prone to additional Vo's in the neighbourhood of the monovalent atoms, resulting in lattice disorder. The Urbach energy, E_u , of the system can be used to estimate such disorder. In comparison to S0 (178.72 meV), the E_u decreases for S1 (130.74 meV) and S2 (88.25 meV), then increases for S3 (185.30 meV), S4 (285.63 meV), and eventually far more for S5 (476.09 meV) [Figure 3.10 (e)].

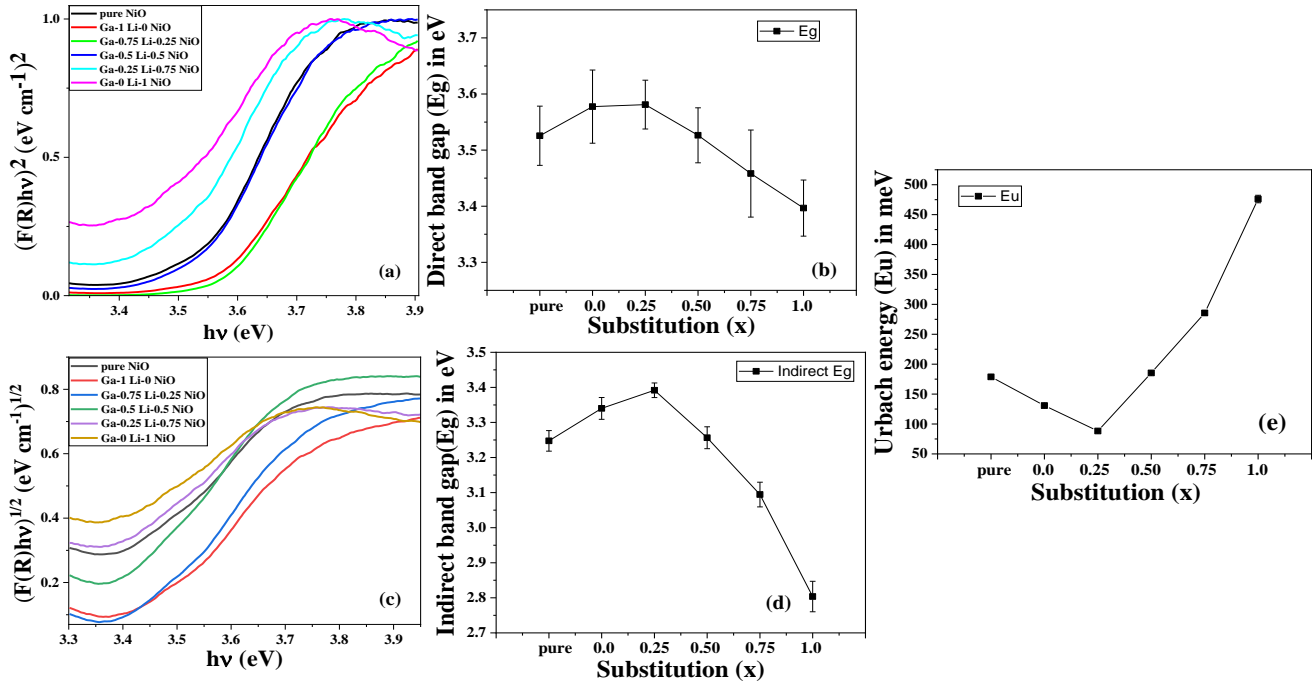


Figure 3.10 (a) Tauc plot for direct band gap (b) Variation in direct band gap energy (c) Tauc plot for indirect band gap (d) Variation in indirect band gap energy (e) Variation in Urbach energy.

3.2.4 Pressure dependent I-V characteristics: -



(a)

(b)

Figure 3.11 (a) Uni-axial Hydraulic Press for making pellets (b) Keithley 2450 Source Meter

The pressure-dependent ($1-3 \text{ ton/cm}^2$) I-V characteristics of all the prepared samples were investigated [Figure 3.12 (a-f)]. The results were repeatable, and the experiment was repeated on the same sample numerous times before being repeated on different specimens of the same composition. For the S0 sample, the differences are minor. The current rose continuously with applied pressure from S0 to S5 at 1.0 V applied voltage. It's also worth noting that the current rises steadily from S0 through S1, S2, and S3, before rapidly increasing for S4 and S5. For S0, S1, S2, and S3, the modifications are insignificant [Figure 3.12]. However, the effects of adding extra Li^+ appear to be dramatic. As a result, it becomes clear that greater quantities of Li^+ ions play a key role in improving charge transfer in the presence of pressure, which could be attributable to contributions from modified Ni^{2+} ion electron clouds due to Li^+ ion doping and therefore the presence of V_o 's. The quantity of current generated owing to pressure in the S1 and S2 samples is less than in the S0 sample, indicating that as Ga^{3+} incorporation increases, conductivity

decreases due to an increase in O_i . As a result, it is clear that increasing V_{os} in the lattice improves conductivity.

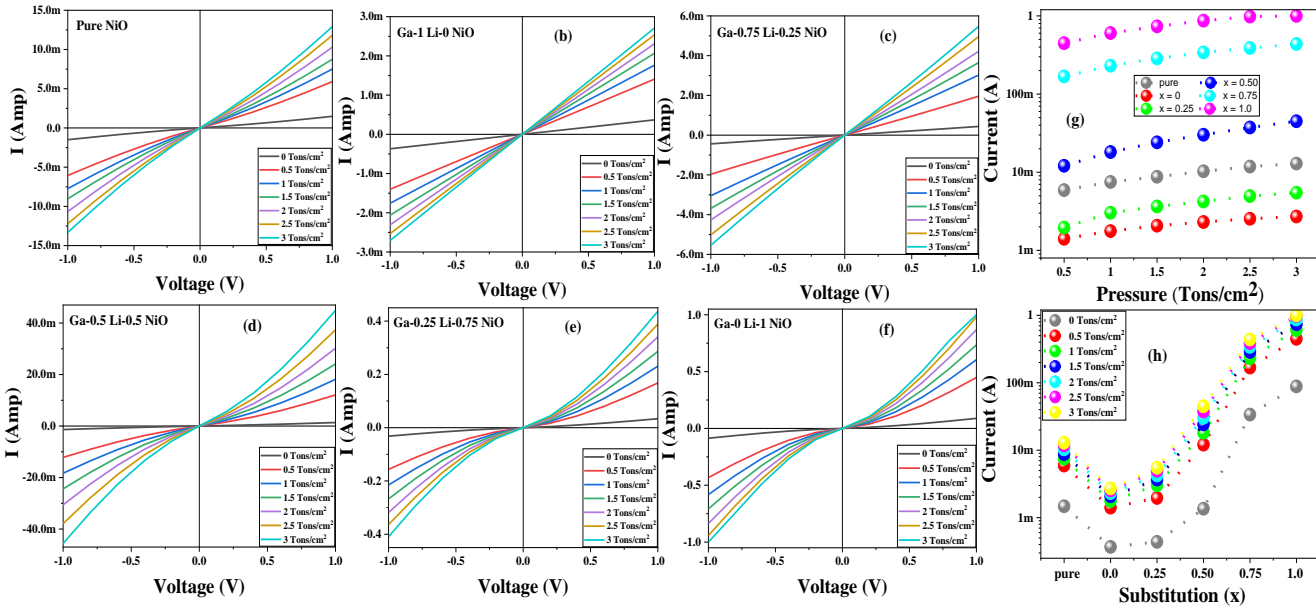


Figure 3.12 Pressure dependent current vs voltage plots (I - V characteristics) for $Ni_{0.9844}(Ga_{1-x}Li_x)_{0.0156}O$.

Summary of this chapter

NiO nanostructures prepared using hydrothermal method gave quite positive results with pure NiO phase formed at 450 °C. It can also be seen that just by varying some of the precursor elements used, nanostructures of different morphology can be obtained. Sol-gel prepared $\text{Ni}_{0.9844}(\text{Ga}_{1-x}\text{Li}_x)_{0.0156}\text{O}$ nanoparticles revealed a cubic *NiO* structure of phase group ($\text{Fm}\bar{3}\text{m}$). The host cation being Ni^{2+} , the Ga^{3+} doped system is an oxygen rich system due to the extra positive charge of Ga^{3+} as compared to Ni^{2+} . Gradual substitution of Ga^{3+} by Li^+ in the Ga^{3+} doped *NiO* system reveals a transformation from an oxygen rich to an oxygen deprived lattice in the modified samples. This increases strain in the lattice upto the point where Ga^{3+} is still present in the lattice. The Ga^{3+} being completely removed, the Li^+ manages to introduce a huge amount of oxygen vacancies which in turn releases the lattice strain due to the larger size of the Li^+ ion. The hybridization of the Li^+ ion with the neighboring anions result in several new energy level creations inside the band gap which act as excitation centers and are revealed by absorption studies. The application of pressure was found to modify the electronic properties most probably due to modifications in the electronic clouds of molecular orbitals. Such modifications increase the conductive properties of the materials.

Chapter 4

Conclusion

Conclusion and Future Work Plans

Contribution of this thesis

The notable contribution of the thesis is in understanding the structure, opto-electronic, and electrical properties of NiO nanostructures and Ga/Li-doped NiO:

- Different morphological nanostructures obtained simply by changing one of the precursors during hydrothermal method.
- A large enhancement in electric properties in antiferromagnetic NiO is achieved with simultaneous substitution of Ga and Li for Ni site.
- In this work, it is also proved that a slightly increased Li doping concentration in NiO can result in a more conducting state compared to Ga doped NiO.

Future directions

The goal of this present study was to investigate the structure correlated characteristics along with electrical properties of simple oxides. The research outcome of the thesis can be expanded to the next level.

- Effect of Li^+/Ga^{3+} can be investigated on the spin-phonon coupling in *NiO* compounds. Ga/Li doped NiO can be further explored as a promising material for energy storage applications.
- Magnetodielectric properties and electrochemical study may be explored in the future.
- There are a lot of scopes to investigate the magneto transport and magnetocaloric properties of these simple oxides in the bulk as well as in single crystal or in thin films.
- In the future, thin films can be prepared from the bulk samples, which may yield better physical properties and ultimately lead to device applications.

References

- [1] K. Nguyen, N. D. Hoa, C. M. Hung, D. T. Thanh Le, N. van Duy, and N. van Hieu, “A comparative study on the electrochemical properties of nanoporous nickel oxide nanowires and nanosheets prepared by a hydrothermal method,” *RSC Advances*, vol. 8, no. 35, pp. 19449–19455, 2018, doi: 10.1039/c8ra02862a.
- [2] L. Wang, Y. Hao, Y. Zhao, Q. Lai, and X. Xu, “Hydrothermal synthesis and electrochemical performance of NiO microspheres with different nanoscale building blocks,” *Journal of Solid State Chemistry*, vol. 183, no. 11, pp. 2576–2581, Nov. 2010, doi: 10.1016/j.jssc.2010.09.006.
- [3] R. Paulose, R. Mohan, and V. Parihar, “Nanostructured nickel oxide and its electrochemical behaviour—A brief review,” *Nano-Structures and Nano-Objects*, vol. 11. Elsevier B.V., pp. 102–111, Jul. 01, 2017. doi: 10.1016/j.nanoso.2017.07.003.
- [4] R. S. Kate, S. A. Khalate, and R. J. Deokate, “Overview of nanostructured metal oxides and pure nickel oxide (NiO) electrodes for supercapacitors: A review,” *Journal of Alloys and Compounds*, vol. 734. Elsevier Ltd, pp. 89–111, Feb. 15, 2018. doi: 10.1016/j.jallcom.2017.10.262.
- [5] F. Taghizadeh, “The Study of Structural and Magnetic Properties of NiO Nanoparticles,” *Optics and Photonics Journal*, vol. 06, no. 08, pp. 164–169, 2016, doi: 10.4236/opj.2016.68b027.
- [6] S. G. Danjumma, Y. Abubakar, and S. Suleiman, “Nickel Oxide (NiO) Devices and Applications: A Review.” [Online]. Available: www.ijert.org
- [7] H. A. Ariyanta, T. A. Ivandini, and Y. Yulizar, “Novel NiO nanoparticles via phytosynthesis method: Structural, morphological

- and optical properties,” *Journal of Molecular Structure*, vol. 1227, Mar. 2021, doi: 10.1016/j.molstruc.2020.129543.
- [8] F. Davar, Z. Fereshteh, and M. Salavati-Niasari, “Nanoparticles Ni and NiO: Synthesis, characterization and magnetic properties,” *Journal of Alloys and Compounds*, vol. 476, no. 1–2, pp. 797–801, May 2009, doi: 10.1016/j.jallcom.2008.09.121.
- [9] J. Osorio-Guillén, S. Lany, and A. Zunger, “Nonstoichiometry and hole doping in NiO,” in *AIP Conference Proceedings*, 2009, vol. 1199, pp. 128–129. doi: 10.1063/1.3295330.
- [10] I. Ardelean, “MAGNETIC SUSCEPTIBILITY INVESTIGATION OF NiO Bi₂O₃ GeO₂ GLASSES,” 2001. [Online]. Available: www.worldscientific.com
- [11] F. Fii~vet, P. Germi, F. de Bergevin, and M. Figlarz, “Lattice Parameter, Microstrains and Non-Stoichiometry in NiO. Comparison between Mosaic Microcrystals and Quasi-Perfect Single Microcrystals,” 1979.
- [12] K. Anandan and V. Rajendran, “Morphological and size effects of NiO nanoparticles via solvothermal process and their optical properties,” *Materials Science in Semiconductor Processing*, vol. 14, no. 1, pp. 43–47, Mar. 2011, doi: 10.1016/j.mssp.2011.01.001.
- [13] *, Yang-Ming Lub, Weng-Sing Hwanga Hao-Long Chena, *Surface & Coatings Technology* 198. 2005.
- [14] M. Nolan, R. Long, N. J. English, and D. A. Mooney, “Hybrid density functional theory description of N- and C-doping of NiO,” *Journal of Chemical Physics*, vol. 134, no. 22, Jun. 2011, doi: 10.1063/1.3596949.

- [15] V. I. Anisimov, J. Zaanen, and O. K. Andersen, “Band theory and Mott insulators: Hubbard U instead of Stoner I.”
- [16] S. L. Dudarev, G. A. Botton, S. Y. Savrasov, C. J. Humphreys, and A. P. Sutton, “Electron-energy-loss spectra and the structural stability of nickel oxide: An LSDAU study,” 1998.
- [17] A. Gandhi and S. Wu, “Strong Deep-Level-Emission Photoluminescence in NiO Nanoparticles,” *Nanomaterials*, vol. 7, no. 8, p. 231, Aug. 2017, doi: 10.3390/nano7080231.
- [18] W. Wang, L. Wang, H. Shi, and Y. Liang, “A room temperature chemical route for large scale synthesis of sub-15 nm ultralong CuO nanowires with strong size effect and enhanced photocatalytic activity,” *CrystEngComm*, vol. 14, no. 18, pp. 5914–5922, Sep. 2012, doi: 10.1039/c2ce25666e.
- [19] T. Serin, A. Yildiz, S. Horzum Ahin, and N. Serin, “Extraction of important electrical parameters of CuO,” *Physica B: Condensed Matter*, vol. 406, no. 3, pp. 575–578, Feb. 2011, doi: 10.1016/j.physb.2010.11.044.
- [20] J. Park, J. Joo, G. K. Soon, Y. Jang, and T. Hyeon, “Synthesis of monodisperse spherical nanocrystals,” *Angewandte Chemie - International Edition*, vol. 46, no. 25, pp. 4630–4660, 2007. doi: 10.1002/anie.200603148.
- [21] A. Madhavi, G. S. Harish, and P. S. Reddy, “Effect of Annealing Temperature on Optical and Electrical Properties of Electron Beam Evaporated NiO Thin Films,” 2016. [Online]. Available: www.ijste.org
- [22] M. Napari, T. N. Huq, R. L. Z. Hoye, and J. L. MacManus-Driscoll, “Nickel oxide thin films grown by chemical deposition techniques: Potential and challenges in next-generation rigid and flexible device

- applications,” *InfoMat*, vol. 3, no. 5. Blackwell Publishing Ltd, pp. 536–576, May 01, 2021. doi: 10.1002/inf2.12146.
- [23] A. Diallo *et al.*, “Structural, optical and photocatalytic applications of biosynthesized nio nanocrystals,” *Green Chemistry Letters and Reviews*, vol. 11, no. 2, pp. 166–175, Apr. 2018, doi: 10.1080/17518253.2018.1447604.
- [24] D. di Girolamo *et al.*, “Progress, highlights and perspectives on NiO in perovskite photovoltaics,” *Chemical Science*, vol. 11, no. 30. Royal Society of Chemistry, pp. 7746–7759, Aug. 14, 2020. doi: 10.1039/d0sc02859b.
- [25] S. W. Park, J. M. Choi, E. Kim, and S. Im, “Inverted top-emitting organic light-emitting diodes using transparent conductive NiO electrode,” in *Applied Surface Science*, May 2005, vol. 244, no. 1–4, pp. 439–443. doi: 10.1016/j.apsusc.2004.10.099.
- [26] S. Liu, R. Liu, Y. Chen, S. Ho, J. H. Kim, and F. So, “Nickel oxide hole injection/transport layers for efficient solution-processed organic light-emitting diodes,” *Chemistry of Materials*, vol. 26, no. 15, pp. 4528–4534, Aug. 2014, doi: 10.1021/cm501898y.
- [27] J. A. Dawson, Y. Guo, and J. Robertson, “Energetics of intrinsic defects in NiO and the consequences for its resistive random access memory performance,” *Applied Physics Letters*, vol. 107, no. 12, Sep. 2015, doi: 10.1063/1.4931751.
- [28] A. J. Haider, R. Al-Anbari, H. M. Sami, and M. J. Haider, “Photocatalytic Activity of Nickel Oxide,” *Journal of Materials Research and Technology*, vol. 8, no. 3, pp. 2802–2808, May 2019, doi: 10.1016/j.jmrt.2019.02.018.
- [29] M. Ramesh, M. P. C. Rao, S. Anandan, and H. Nagaraja, “Adsorption and photocatalytic properties of NiO nanoparticles

- synthesized via a thermal decomposition process,” *Journal of Materials Research*, vol. 33, no. 5, pp. 601–610, Mar. 2018, doi: 10.1557/jmr.2018.30.
- [30] C. H. Lai, M. Y. Lu, and L. J. Chen, “Metal sulfide nanostructures: Synthesis, properties and applications in energy conversion and storage,” *Journal of Materials Chemistry*, vol. 22, no. 1, pp. 19–30, Jan. 2012, doi: 10.1039/c1jm13879k.
- [31] J. Jiang, Y. Li, J. Liu, X. Huang, C. Yuan, and X. W. Lou, “Recent advances in metal oxide-based electrode architecture design for electrochemical energy storage,” *Advanced Materials*, vol. 24, no. 38, pp. 5166–5180, Oct. 02, 2012. doi: 10.1002/adma.201202146.
- [32] B. Wang, J. S. Chen, H. bin Wu, Z. Wang, and X. W. Lou, “Quasiemulsion-templated formation of α -Fe₂O₃ hollow spheres with enhanced lithium storage properties,” *J Am Chem Soc*, vol. 133, no. 43, pp. 17146–17148, Nov. 2011, doi: 10.1021/ja208346s.
- [33] Q. F. , S. W. 1, I. N. , M. N. , K. S. MATSUMIYA M., “THIN-FILM LI-DOPED NIO FOR THERMOELECTRIC HYDROGEN GAS SENSOR,” *THIN SOLID FILMS*, vol. 419, pp. 213–217, 2002.
- [34] J. Y. So, C. H. Lee, J. E. Kim, H. J. Kim, J. Jun, and W. G. Bae, “Hierarchically nanostructured CuO-Cu current collector fabricated by hybrid methods for developed Li-Ion batteries,” *Materials*, vol. 11, no. 6, Jun. 2018, doi: 10.3390/ma11061018.
- [35] J. Philip, P. D. Shima, and B. Raj, “Nanofluid with tunable thermal properties,” *Applied Physics Letters*, vol. 92, no. 4, 2008, doi: 10.1063/1.2838304.
- [36] V. Mahendran and J. Philip, “Nanofluid based optical sensor for rapid visual inspection of defects in ferromagnetic materials,”

- Applied Physics Letters*, vol. 100, no. 7, Feb. 2012, doi: 10.1063/1.3684969.
- [37] S. Kralj, M. Rojnik, J. Kos, and D. Makovec, “Targeting EGFR-overexpressed A431 cells with EGF-labeled silica-coated magnetic nanoparticles,” *Journal of Nanoparticle Research*, vol. 15, no. 5, May 2013, doi: 10.1007/s11051-013-1666-6.
- [38] T. Hyeon, “Chemical synthesis of magnetic nanoparticles,” *Chemical Communications*, vol. 3, no. 8, pp. 927–934, 2003, doi: 10.1039/b207789b.
- [39] S. Mornet *et al.*, “Magnetic nanoparticle design for medical applications,” *Progress in Solid State Chemistry*, vol. 34, no. 2–4, pp. 237–247, 2006, doi: 10.1016/j.progsolidstchem.2005.11.010.
- [40] N. D. Jaji, H. L. Lee, M. H. Hussin, H. M. Akil, M. R. Zakaria, and M. B. H. Othman, “Advanced nickel nanoparticles technology: From synthesis to applications,” *Nanotechnology Reviews*, vol. 9, no. 1. De Gruyter Open Ltd, pp. 1456–1480, Jan. 01, 2020. doi: 10.1515/ntrev-2020-0109.
- [41] K. P. Raj, V. Thangaraj, and A. P. Uthirakumar, “Chemical Science Review and Letters Synthetic Routes to Nickel Oxide Nanoparticles-An Overview,” *Chem Sci Rev Lett*, vol. 2015, no. 14.
- [42] G. Qian, Q. Peng, D. Zou, S. Wang, and B. Yan, “Hydrothermal Synthesis of Flake-Flower NiO and Its Gas Sensing Performance to CO,” *Frontiers in Materials*, vol. 7, Aug. 2020, doi: 10.3389/fmats.2020.00216.
- [43] J. L. Hodeau and R. Guinebretiere, “Crystallography: Past and present,” *Applied Physics A: Materials Science and Processing*, vol. 89, no. 4, pp. 813–823, Dec. 2007, doi: 10.1007/s00339-007-4223-2.

- [44] Carmelo. Giacovazzo, *Fundamentals of crystallography*. International Union of Crystallography, 1992.
- [45] S. C. Vogel, "Gsaslanguage: A GSAS script language for automated Rietveld refinements of diffraction data," *Journal of Applied Crystallography*, vol. 44, no. 4, pp. 873–877, Aug. 2011, doi: 10.1107/S0021889811023181.
- [46] H. M. Rietveld, "A Profile Refinement Method for Nuclear and Magnetic Structures," 1969.
- [47] D. A. Long, "Handbook of Raman spectroscopy. From the research laboratory to the process line. Edited by Ian R. Lewis and Howell G. M. Edwards. Marcel Dekker, New York and Basel, 2001. Price\$225.," *Journal of Raman Spectroscopy*, vol. 35, no. 1, pp. 91–91, Jan. 2004, doi: 10.1002/jrs.1117.
- [48] H. van B. A. C. F. S. Jiri Cejka, *Introduction to Zeolite Molecular Sieves*, 3rd Revised Edition. 2007.
- [49] J. R. Ferraro, K. Nakamoto, and C. W. Brown, *Introductory Raman spectroscopy*. Academic Press, 2003.
- [50] E. Smith and G. Dent, "Modern Raman Spectroscopy-A Practical Approach."
- [51] D. F. F. Swinehart, *The Beer-Lambert Law*, vol. Vol. 39 (7). Journal of chemical education, 1962.
- [52] L. Yang and B. Rn Kruse, "Revised Kubelka-Munk theory. I. Theory and application," 2004.
- [53] E. Kim, Z.-T. Jiang, and K. No, "Measurement and Calculation of Optical Band Gap of Chromium Aluminum Oxide Films," 2000. [Online]. Available: <http://iopscience.iop.org/1347-4065/39/8R/4820>

- [54] Tauc, *AMORPHOUS AND LIQUID SEMICONDUCTORS Edited by PLENUM PRESS. LONDON AND NEW YORK. 1974. 1974.*
- [55] E. Aytan *et al.*, “Spin-phonon coupling in antiferromagnetic nickel oxide,” *Applied Physics Letters*, vol. 111, no. 25, Dec. 2017, doi: 10.1063/1.5009598.
- [56] R. Shanaj Begum and R. J. J. Xavier, “ARTICLE INFO Article history: Effect of Lithium doping on Structural, Optical, Electrochemical and Magnetic Properties of NiO Nanoparticles,” 2016. [Online]. Available: www.elixirpublishers.com
- [57] M. Taeño, D. Maestre, J. Ramírez-Castellanos, S. Li, P. S. Lee, and A. Cremades, “Towards control of the size, composition and surface area of nio nanostructures by sn doping,” *Nanomaterials*, vol. 11, no. 2, pp. 1–13, Feb. 2021, doi: 10.3390/nano11020444.